High-Q^2 neutral current cross sections in $e^+ p$ deep inelastic scattering at $\sqrt{s} = 318$ GeV

S. Chekanov, M. Derrick, D. Krakauer, J. H. Loizides,[a] S. Magill, S. Miglioranzi,[a] B. Musgrave,
J. Repond, and R. Yoshida
Argonne National Laboratory, Argonne, Illinois 60439-4815, USA

M. C. K. Mattingly
Andrews University, Berrien Springs, Michigan 49104-0380, USA

P. Antonioli, G. Bari, M. Basile, L. Bellagamba, D. Boscherini, A. Bruni, G. Bruni, G. Cara Romeo, L. Cifarelli,
F. Cindolo, A. Contin, M. Corradi, S. De Pasquale, P. Giusti, G. Iacobucci, A. Margotti, A. Montanari, R. Nania,
F. Palmonari, A. Pesci, G. Sartorelli, and A. Zichichi
University and INFN Bologna, Bologna, Italy

G. Aghuzumtsyan, D. Bartsch, I. Brock, S. Goers, H. Hartmann, E. Hilger, P. Irrgang, H.-P. Jakob, A. Kappes,[b] O. Kind,
U. Meyer, E. Paul,[c] J. Rautenberg, R. Renner, H. Schnurbusch,[d] A. Stifutkin, J. Tandler, K. C. Voss,
M. Wang, and A. Weber[e]
Physikalisches Institut der Universität Bonn, Bonn, Germany

D. S. Bailey, N. H. Brook, J. E. Cole, G. P. Heath, T. Namsoo, S. Robins, and M. Wing
H.H. Wills Physics Laboratory, University of Bristol, Bristol, United Kingdom

M. Capua, A. Mastroberardino, M. Schioppa, and G. Susinno
Physics Department and INFN, Calabria University, Cosenza, Italy

J. Y. Kim, Y. K. Kim, J. H. Lee, I. T. Lim, and M. Y. Pac[f]
Chonnam National University, Kwangju, Korea

A. Caldwell,[g] M. Helbich, X. Liu, B. Mellado, Y. Ning, S. Paganis, Z. Ren, W. B. Schmidke, and F. Sciulli
Nevis Laboratories, Columbia University, Irvington on Hudson, New York 10027, USA

J. Chwastowski, A. Eskreys, J. Figiel, A. Galas, K. Olkiewicz, P. Stopa, and L. Zawiejski
Institute of Nuclear Physics, Cracow, Poland

L. Adamczyk, T. Bołd, I. Grabowska-Bołd, D. Kisielewska, A. M. Kowal, M. Kowal, T. Kowalski, M. Przybycień,
L. Suszycki, D. Szuba, and J. Szuba
Faculty of Physics and Nuclear Techniques, AGH-University of Science and Technology, Cracow, Poland

A. Kotański and W. Słomiński
Department of Physics, Jagellonian University, Cracow, Poland

V. Adler, U. Behrens, I. Bloch, K. Borras, V. Chiochia, D. Dannheim, G. Drews, J. Fourletova, U. Fricke, A. Geiser,
P. Göttlicher,[h] O. Gutsche, T. Haas, W. Hain, S. Hillert,[i] B. Kahle, U. Kötz, H. Kowalski,[j] G. Kramberger, H. Labes,
D. Lelas, H. Lim, B. Löhr, R. Mankel, I.-A. Melzer-Pellmann, M. Moritz,[k] C. N. Nguyen, D. Notz,
A. E. Nuncio-Quiroz, A. Polini, A. Raval, L. Rurua, U. Schneekloth, U. Stösslein, G. Wolf, C. Youngman, and W. Zeuner
Deutsches Elektronen-Synchrotron DESY, Hamburg, Germany

A. Lopez-Duran Viani[l] and S. Schlenstedt
DESY Zeuthen, Zeuthen, Germany

G. Barbagli, E. Gallo, C. Genta, and P. G. Pelfer
University and INFN, Florence, Italy

A. Bamberger, A. Benen, F. Karstens, D. Dobur, and N. N. Vlasov
Fakultät für Physik der Universität Freiburg i.Br., Freiburg i.Br., Germany

M. Bell, P. J. Bussey, A. T. Doyle, J. Ferrando, J. Hamilton, S. Hanlon, D. H. Saxon, and I. O. Skillicorn
Department of Physics and Astronomy, University of Glasgow, Glasgow, United Kingdom

70 052001-1

I. Gialas

Department of Engineering in Management and Finance, University of Aegean, Greece

T. Carli, T. Gosau, U. Holm, N. Krumnack, E. Lohrmann, M. Milite, H. Salehi, P. Schleper, S. Stonjek,[i] K. Wichmann, K. Wick, A. Ziegler, and Ar. Ziegler

Institute of Experimental Physics, Hamburg University, Hamburg, Germany

C. Collins-Tooth, C. Foudas, R. Gonçalo,[m] K. R. Long, and A. D. Tapper

High Energy Nuclear Physics Group, Imperial College London, London, United Kingdom

P. Cloth and D. Filges

Forschungszentrum Jülich, Institut für Kernphysik, Jülich, Germany

M. Kataoka,[n] K. Nagano, K. Tokushuku,[o] S. Yamada, and Y. Yamazaki

Institute of Particle and Nuclear Studies, KEK, Tsukuba, Japan

A. N. Barakbaev, E. G. Boos, N. S. Pokrovskiy, and B. O. Zhautykov

Institute of Physics and Technology of Ministry of Education and Science of Kazakhstan, Almaty, Kazakhstan

D. Son

Center for High Energy Physics, Kyungpook National University, Daegu, South Korea

K. Piotrzkowski

Institut de Physique Nucléaire, Université Catholique de Louvain, Louvain-la-Neuve, Belgium

F. Barreiro, C. Glasman, O. González, L. Labarga, J. del Peso, E. Tassi, J. Terrón, M. Vázquez, and M. Zambrana

Departamento de Física Teórica, Universidad Autónoma de Madrid, Madrid, Spain

M. Barbi, F. Corriveau, S. Gliga, J. Lainesse, S. Padhi, D. G. Stairs, and R. Walsh

Department of Physics, McGill University, Montréal, Québec, Canada H3A 2T8

T. Tsurugai

Faculty of General Education, Meiji Gakuin University, Yokohama, Japan

A. Antonov, P. Danilov, B. A. Dolgoshein, D. Gladkov, V. Sosnovtsev, and S. Suchkov

Moscow Engineering Physics Institute, Moscow, Russia

R. K. Dementiev, P. F. Ermolov, Yu. A. Golubkov,[p] I. I. Katkov, L. A. Khein, I. A. Korzhavina, V. A. Kuzmin, B. B. Levchenko, O. Yu. Lukina, A. S. Proskuryakov, L. M. Shcheglova, and S. A. Zotkin

Institute of Nuclear Physics, Moscow State University, Moscow, Russia

N. Coppola, S. Grijpink, E. Koffeman, P. Kooijman, E. Maddox, A. Pellegrino, S. Schagen, H. Tiecke, J. J. Velthuis, L. Wiggers, and E. de Wolf

NIKHEF and University of Amsterdam, Amsterdam, Netherlands

N. Brümmer, B. Bylsma, L. S. Durkin, and T. Y. Ling

Physics Department, Ohio State University, Columbus, Ohio 43210, USA

A. M. Cooper-Sarkar, A. Cottrell, R. C. E. Devenish, B. Foster, G. Grzelak, C. Gwenlan, S. Patel, P. B. Straub, and R. Walczak

Department of Physics, University of Oxford, Oxford United Kingdom

A. Bertolin, R. Brugnera, R. Carlin, F. Dal Corso, S. Dusini, A. Garfagnini, S. Limentani, A. Longhin, A. Parenti, M. Posocco, L. Stanco, and M. Turcato

Dipartimento di Fisica dell' Università and INFN, Padova, Italy

E. A. Heaphy, F. Metlica, B. Y. Oh, and J. J. Whitmore[q]

Department of Physics, Pennsylvania State University, University Park, Pennsylvania 16802, USA

Y. Iga

Polytechnic University, Sagamihara, Japan

G. D'Agostini, G. Marini, and A. Nigro

Dipartimento di Fisica, Università "La Sapienza" and INFN, Rome, Italy

C. Cormack,[r] J. C. Hart, and N. A. McCubbin

Rutherford Appleton Laboratory, Chilton, Didcot, Oxon, United Kingdom

C. Heusch

University of California, Santa Cruz, California 95064, USA

I. H. Park

Department of Physics, Ewha Womans University, Seoul, Korea

N. Pavel

Fachbereich Physik der Universität-Gesamthochschule Siegen, Germany

H. Abramowicz, A. Gabareen, S. Kananov, A. Kreisel, and A. Levy

Raymond and Beverly Sackler Faculty of Exact Sciences, School of Physics, Tel-Aviv University, Tel-Aviv, Israel

M. Kuze

Department of Physics, Tokyo Institute of Technology, Tokyo, Japan

T. Fusayasu, S. Kagawa, T. Kohno, T. Tawara, and T. Yamashita

Department of Physics, University of Tokyo, Tokyo, Japan

R. Hamatsu, T. Hirose,[c] M. Inuzuka, H. Kaji, S. Kitamura,[s] and K. Matsuzawa

Department of Physics, Tokyo Metropolitan University, Tokyo, Japan

M. I. Ferrero, V. Monaco, R. Sacchi, and A. Solano

Università di Torino and INFN, Torino, Italy

M. Arneodo and M. Ruspa

Università del Piemonte Orientale, Novara, and INFN, Torino, Italy

T. Koop, J. F. Martin, and A. Mirea

Department of Physics, University of Toronto, Toronto, Ontario, Canada M5S 1A7

J. M. Butterworth, R. Hall-Wilton, T. W. Jones, M. S. Lightwood, M. R. Sutton, and C. Targett-Adams

Physics and Astronomy Department, University College London, London, United Kingdom

J. Ciborowski,[t] R. Ciesielski, P. Łużniak,[u] R. J. Nowak, J. M. Pawlak, J. Sztuk, T. Tymieniecka, A. Ukleja, J. Ukleja, and A. F. Żarnecki

Institute of Experimental Physics, Warsaw University, Warsaw, Poland

M. Adamus and P. Plucinski

Institute for Nuclear Studies, Warsaw, Poland

Y. Eisenberg, L. K. Gladilin,[v] D. Hochman, U. Karshon, and M. Riveline

Department of Particle Physics, Weizmann Institute, Rehovot, Israel

D. Kçira, S. Lammers, L. Li, D. D. Reeder, M. Rosin, A. A. Savin, and W. H. Smith

Department of Physics, University of Wisconsin, Madison, Wisconsin 53706, USA

A. Deshpande and S. Dhawan

Department of Physics, Yale University, New Haven, Connecticut 06520-8121, USA

S. Bhadra, C. D. Catterall, S. Fourletov, G. Hartner, S. Menary, M. Soares, and J. Standage

Department of Physics, York University, Ontario, Canada M3J 1P3

(Zeus Collaboration)

Cross sections for $e^+ p$ neutral current deep inelastic scattering have been measured at a center-of-mass energy of $\sqrt{s} = 318$ GeV with the ZEUS detector at HERA using an integrated luminosity of 63.2 pb^{-1}. The double-differential cross section, $d^2\sigma/dxdQ^2$, is presented for 200 GeV$^2 < Q^2 <$ 30 000 GeV^2 and for $0.005 < x < 0.65$. The single-differential cross sections $d\sigma/dQ^2$, $d\sigma/dx$ and $d\sigma/dy$ are presented for $Q^2 > 200$ GeV^2. The effect of Z-boson-exchange is seen in $d\sigma/dx$ measured for $Q^2 > 10\,000$ GeV^2. The data presented here were combined with ZEUS $e^+ p$ neutral current data taken at $\sqrt{s} = 300$ GeV and the structure function F_2^{em} was extracted. All results agree well with the predictions of the Standard Model.

I. INTRODUCTION

Neutral current (NC) deep inelastic scattering (DIS) is described in terms of the spacelike exchange of a virtual photon and a virtual Z boson. The photon-exchange contribution dominates when the four-momentum-transfer squared, Q^2, is much less than the square of the Z-boson mass, M_Z^2. The effect of Z exchange is comparable in magnitude to that of photon exchange when $Q^2 \sim M_Z^2$. The parity-violating part of the Z exchange contribution increases the cross section for $e^- p$ NC DIS and decreases that for $e^+ p$ NC DIS over what would be expected for pure single-photon exchange. The comparison of the $e^- p$ NC DIS cross section to that for $e^+ p$ NC DIS therefore provides a direct way to observe the effect of Z exchange in the scattering of charged leptons on protons.

The ZEUS and H1 collaborations have each measured both the $e^- p$ and the $e^+ p$ NC DIS cross sections up to a Q^2 of 30 000 GeV^2 [1–9]. When HERA ran at a center-of-mass energy $\sqrt{s} = 300$ GeV, $e^+ p$ data sets were collected, whereas both $e^+ p$ and $e^- p$ data were collected in 199–2000 at $\sqrt{s} = 318$ GeV. The measured $e^\pm p$ NC DIS cross sections are well described at next-to-leading order (NLO) in quantum chromodynamics (QCD) by the Standard Model (SM) prediction including both photon- and Z-exchange contributions.

This paper presents the measurement of the NC $e^+ p$ DIS cross section $d^2\sigma/dxdQ^2$ for 200 GeV$^2 < Q^2 <$ 30 000 GeV^2 and $0.005 < x < 0.65$, together with $d\sigma/dQ^2$, $d\sigma/dx$ and $d\sigma/dy$ for $Q^2 > 200$ GeV^2, where x and y are the Bjorken scaling variables. The data were collected in 1999 and 2000 at $\sqrt{s} = 318$ GeV and correspond to an integrated luminosity of 63.2 pb^{-1}. The results are compared to recent ZEUS measurements of the $e^- p$ NC DIS cross sections [5] and to SM predictions. The structure function F_2^{em} was extracted by combining the data presented here with the ZEUS measurement of $d^2\sigma/dxdQ^2$ for NC DIS at $\sqrt{s} = 300$ GeV [4], and compared to measurements by the H1 collaboration and by fixed-target experiments.

$^{\text{a}}$Also affiliated with University College London, London, UK.
$^{\text{b}}$Now at University of Erlangen-Nürnberg, Germany.
$^{\text{c}}$Retired.
$^{\text{d}}$Now at Sparkasse Köln.
$^{\text{e}}$Self-employed.
$^{\text{f}}$Now at Dongshin University, Naju, Korea.
$^{\text{g}}$Now at Max-Planck-Institut für Physik, München, Germany.
$^{\text{h}}$Now at DESY group FEB.
$^{\text{i}}$Now at University of Oxford, Oxford, UK.
$^{\text{j}}$On leave of absence at Columbia University, Nevis Laboratories, NY, USA.
$^{\text{k}}$Now at CERN.
$^{\text{l}}$Now at Deutsche Börse Systems AG, Frankfurt, Main, Germany.
$^{\text{m}}$Now at Royal Holloway University of London, London, UK.
$^{\text{n}}$Also at Nara Women's University, Nara, Japan.
$^{\text{o}}$Also at University of Tokyo, Tokyo, Japan.
$^{\text{p}}$Now at HERA-B.
$^{\text{q}}$On leave of absence at The National Science Foundation, Arlington, VA, USA.
$^{\text{r}}$Now at University of London, Queen Mary College, London, UK.
$^{\text{s}}$Present address: Tokyo Metropolitan University of Health Sciences, Tokyo 116-8551, Japan.
$^{\text{t}}$Also at Łódź University, Poland.
$^{\text{u}}$Łódź University, Poland.
$^{\text{v}}$On leave from MSU.

II. STANDARD MODEL CROSS SECTIONS

For longitudinally unpolarized beams, the NC DIS differential cross section, $d^2\sigma_{\text{Born}}/dxdQ^2$, for the reaction $e^+ p \rightarrow e^+ X$ can be written at leading order in the electroweak interaction as [10,11]:

$$\frac{d^2\sigma_{\text{Born}}(e^\pm p)}{dxdQ^2} = \frac{2\pi\alpha^2}{xQ^4}[Y_+ F_2(x, Q^2) \mp Y_- xF_3(x, Q^2) - y^2 F_L(x, Q^2)], \quad (1)$$

where $y = Q^2/xs$ (neglecting the masses of the incoming

particles) and $Y_\pm \equiv 1 \pm (1-y)^2$ and α denotes the fine-structure constant. At leading order (LO) in QCD, the longitudinal structure function, F_L, is zero and the structure functions F_2 and xF_3 can be expressed as products of electroweak couplings and parton density functions (PDFs) as follows:

$$F_2 = x\sum_f A_f(q_f + \bar{q}_f), \qquad xF_3 = x\sum_f B_f(q_f - \bar{q}_f),$$

where $xq_f(x, Q^2)$ are the quark and $x\bar{q}_f(x, Q^2)$ the anti-quark PDFs and f runs over the five active quark flavors; A_f and B_f contain products of electroweak couplings and ratios of photon and Z-boson propagators. For convenience, the reduced cross section, $\tilde{\sigma}$, can be defined as

$$\tilde{\sigma} = \frac{xQ^4}{2\pi\alpha^2 Y_+} \frac{d^2\sigma_{\text{Born}}}{dxdQ^2}.$$

All cross-section calculations presented in this paper have been performed using NLO QCD. These calculations predict that the contribution of F_L to $d^2\sigma_{\text{Born}}/dxdQ^2$ is approximately 1.5%, averaged over the kinematic range considered in this paper. However, in the region of small x, near $Q^2 = 250$ GeV^2, the F_L contribution to the cross section can be as large as 17%.

III. THE ZEUS EXPERIMENT AT HERA

For the data analyzed in the present study, HERA accelerated positrons to an energy of $E_e = 27.5$ GeV and protons to an energy of $E_p = 920$ GeV, yielding $\sqrt{s} = 318$ GeV. The interbunch spacing of the beams was 96 ns. In normal running, some radiofrequency buckets in both the positron and the proton ring were left empty to study single-beam backgrounds.

A detailed description of the ZEUS detector can be found elsewhere [12]. A brief outline of the components that are most relevant for this analysis is given below.

The high-resolution uranium-scintillator calorimeter (CAL) [13] consists of three parts: the forward (FCAL), the barrel (BCAL) and the rear (RCAL) calorimeters. Each part is subdivided into towers and each tower is longitudinally segmented into one electromagnetic section and either one (in RCAL) or two (in BCAL and FCAL) hadronic sections. The smallest subdivision of the calorimeter is called a cell. The CAL energy resolutions, measured under test-beam conditions, are $\sigma(E)/E = 0.18/\sqrt{E}$ for positrons and $\sigma(E)/E = 0.35/\sqrt{E}$ for hadrons, with E in GeV. The timing resolution of the CAL is ~ 1 ns for energy deposits greater than 4.5 GeV.

Presampler detectors [14] are mounted in front of the CAL. They consist of scintillator tiles matching the calorimeter towers and measure signals from particle showers created by interactions in the material lying between the interaction point and the calorimeter.

The RCAL is instrumented with a layer of 3×3 cm^2 silicon-pad detectors at a depth of 3.3 radiation lengths. This hadron-electron separator (HES) [15] is used to improve the positron-angle measurement.

Charged particles are tracked in the central tracking detector (CTD) [16], which operates in a magnetic field of 1.43 T provided by a thin superconducting solenoid. The CTD consists of 72 cylindrical drift-chamber layers, organized in nine superlayers covering the polar-angle[1] region $15° < \theta < 164°$. The transverse-momentum resolution for full-length tracks is $\sigma(p_T)/p_T = 0.0058p_T \oplus 0.0065 \oplus 0.0014/p_T$, with p_T in GeV.

The luminosity is measured using the Bethe-Heitler reaction $ep \to e\gamma p$ [17]. The resulting small-angle photons were measured by the luminosity monitor, a lead-scintillator calorimeter placed in the HERA tunnel 107 m from the interaction point in the positron beam direction. In addition a lead-scintillator calorimeter placed 35 m from the interaction point was used to measure positrons scattered through small angles.

IV. MONTE CARLO SIMULATION

Monte Carlo (MC) simulations were used to evaluate the efficiency for selecting events, to determine the accuracy of the kinematic reconstruction, to estimate the background rate, and to extrapolate the measured cross sections to the full kinematic range. A sufficient number of events was generated to ensure that statistical uncertainties from the MC samples were negligible in comparison to those of the data.

Neutral current DIS events were simulated including radiative effects, using the HERACLES 4.6.1 [18] program with the DJANGOH 1.1 [19] interface to the hadronization programs and using CTEQ5D [20] PDFs. In HERACLES, $\mathcal{O}(\alpha)$ electroweak corrections for initial- and final-state radiation, vertex and propagator corrections, and two-boson-exchange are included. Values from the Particle Data Group [21] were used for the Fermi constant, G_F, and the masses of the Z boson and the top quark. The Higgs-boson mass was set to 100 GeV. The color-dipole model of ARIADNE 4.10 [22] was used to simulate the $\mathcal{O}(\alpha_S)$ plus leading-logarithmic corrections to the quark-parton model. The MEPS model of LEPTO 6.5 [23] was used as a check. Both programs use the Lund string model of JETSET 7.4 [24] for the hadronization. Diffractive events, characterized by a suppression of particle production between the current jet and the proton

---

[1]The ZEUS coordinate system is a right-handed Cartesian system, with the Z axis pointing in the proton-beam direction, referred to as the "forward direction," and the X axis pointing left towards the center of HERA. The coordinate origin is at the nominal interaction point.

remnant, were generated using the RAPGAP 2.08/06 [25] generator and appropriately mixed with the nondiffractive NC DIS sample. The contribution of diffractive events was obtained by fitting the η_{max} distribution[2] of the data with a linear combination of nondiffractive and diffractive MC samples while preserving the overall normalization. The fraction of diffractive events in the MC sample was 6.2%. Photoproduction events, including both direct and resolved processes, were simulated using HERWIG 6.1 [26] to study backgrounds. The normalization of the photoproduction MC was determined from a sample of events in which the positron was detected in the positron calorimeter of the luminosity monitor [27].

The ZEUS detector response was simulated using a program based on GEANT 3.13 [28]. The generated events were passed through the detector simulation, subjected to the same trigger requirements as the data and processed by the same reconstruction programs.

The vertex distribution in data is a crucial input to the MC simulation for the correct evaluation of the event-selection efficiency. Therefore, the Z-vertex distribution used in the MC simulation was determined from a sample of NC DIS events in which the event-selection efficiency was independent of Z.

V. EVENT CHARACTERISTICS AND KINEMATIC RECONSTRUCTION

Neutral current events at high Q^2 are characterized by the presence of a high-energy isolated positron in the final state. The transverse momentum of the scattered-positron balances that of the hadronic final state, resulting in a small net transverse momentum, P_T. The measured net transverse momentum and the net transverse energy, E_T, are defined by

$$P_T^2 = P_X^2 + P_Y^2$$
$$= \left(\sum_i E_i \sin\theta_i \cos\phi_i \right)^2 + \left(\sum_i E_i \sin\theta_i \sin\phi_i \right)^2, \quad (2)$$
$$E_T = \sum_i E_i \sin\theta_i,$$

where the sums run over all calorimeter energy deposits, E_i, with polar and azimuthal angles θ_i and ϕ_i with respect to the event vertex, respectively. The variable δ is also used in the event selection and is defined as

$$\delta \equiv \sum_i (E - p_Z)_i = \sum_i (E_i - E_i \cos\theta_i) \quad (3)$$

where the sum runs over all calorimeter energy deposits E_i (uncorrected for detector effects in the trigger, but corrected in the offline analysis as discussed below)

---

[2]The quantity η_{max} is defined as the pseudorapidity of the CAL energy deposit with the lowest polar-angle and an energy above 400 MeV.

with polar angles θ_i. Conservation of energy and longitudinal momentum, p_Z, requires $\delta = 2E_e = 55$ GeV if all final-state particles are detected and perfectly measured. Undetected particles that escape through the forward beam hole have a negligible effect on δ. However, particles lost through the rear beam hole can lead to a substantial reduction in δ such as is the case in photoproduction events, in which the positron emerges at very small scattering angles, or in events in which an initial-state bremsstrahlung photon is emitted.

For the present study, the CAL energy deposits were separated into those associated with the scattered positron and all other energy deposits. The sum of the latter is referred to as the hadronic energy. The spatial distribution of the hadronic energy, together with the reconstructed vertex position, were used to evaluate the hadronic polar angle, γ_h (see Sec. VII B), which, in the naive quark-parton model, corresponds to the polar angle of the struck quark.

The reconstruction of x, Q^2 and y was performed using the double angle (DA) method [29]. This method uses the polar angle of the scattered positron and the hadronic angle, γ_h, to obtain estimators of the kinematic variables, xDA, yDA and Q^2DA. The DA method is insensitive to uncertainties in the overall energy scale of the calorimeter. However, it is sensitive to initial-state QED radiation and, in addition, an accurate simulation of the hadronic final state is necessary. In the event selection, y calculated using the electron method (y_e) and the Jacquet-Blondel method [30] (yJB) were also used.

The relative resolution in Q^2 was $\sim$3% over the kinematic range covered. The relative resolution in x varied from 15% in the lowest Q^2 bins (see Sec. IX A) to $\sim$4% in the highest Q^2 region. The relative resolution in y was $\sim$10% in the lowest Q^2 bins, decreasing to 1% for high y values in the highest Q^2 bins.

VI. POSITRON RECONSTRUCTION

A. Positron identification

To identify and reconstruct the scattered positron, an algorithm was used that combines calorimeter and CTD information [1]. The algorithm starts by identifying CAL clusters that are topologically consistent with an electromagnetic shower. The clusters were required to have an energy of at least 10 GeV and, if the positron candidate fell within the acceptance of the CTD, a track was required which, when extrapolated, passed within 10 cm of the cluster center at the shower maximum. Such a track will be referred to as a "matched" track. A positron candidate was considered to lie within the CTD acceptance if a matched track emerging from the reconstructed event vertex traversed at least four of the nine superlayers of the CTD. For the nominal interaction point, i.e. $Z = 0$, this requirement corresponds to the angular range $23° < \theta_e < 156°$. Monte Carlo studies [31] showed that the

overall efficiency for finding the scattered positron is ~95% for a scattered-positron energy, E_e', greater than 10 GeV and $Q^2 < 15\,000$ GeV^2, decreasing to ~85% for $Q^2 > 30\,000$ GeV^2.

B. Positron-energy determination

The scattered-positron energy was determined from the calorimeter deposit since, above 10 GeV, the calorimeter energy resolution is better than the momentum resolution of the CTD. The measured energy was corrected for the energy lost in inactive material in front of the CAL. The presampler was used in the RCAL, while in the B/FCAL a detailed material map was used [4]. To render the energy response uniform across the face of the calorimeter, a correction obtained from fits to the nonuniformity pattern in data and in the MC simulation [1] was made. The corrections were determined separately for the BCAL and the RCAL. After these corrections, the nonuniformities were greatly reduced and the data were well reproduced by the MC simulation [32]. Too few positrons were scattered into the FCAL for such a correction to be derived.

After applying the corrections described above, the positron-energy resolution was 10% at $E_e' = 10$ GeV, falling to 5% for $E_e' \gtrsim 20$ GeV. The scale uncertainty on the energies of the scattered positrons detected in the BCAL was ±1%. For positrons detected in the RCAL, the scale uncertainty was ±1.7% at 10 GeV, falling linearly to ±1% for positrons with energies of 15 GeV and above [4]. A scale uncertainty of ±3% was assigned to positrons reconstructed in the FCAL [1].

C. Determination of the positron polar angle

Studies [33] showed that the angular resolution of tracks is superior to that for calorimeter clusters. Hence, in the CTD acceptance region, which contains 98.8% of the events, θ_e was determined using the matched track. For candidates outside this region, the position of the calorimeter cluster was used together with the event vertex to determine the positron angle.

The CAL was aligned with respect to the CTD using the positron tracks extrapolated to the face of the calorimeter with the aid of a detailed map of the magnetic field. This allowed the BCAL to be aligned to precisions of ±0.3 mm in the Z direction and ±0.6 mrad in the azimuthal angle, ϕ [34]. For the alignment of the RCAL, the position of the extrapolated track was compared to that determined by the HES [34]. The precision of the alignment was ±0.3 mm (± 0.6 mm) in the X (Z) direction and ±0.9 mrad in ϕ. In all cases, the precision was sufficient to render resulting systematic uncertainties on the cross sections negligible.

The resolution in θ_e was obtained by comparing the MC-generated angle to that obtained after applying the detector simulation, reconstruction and correction algo-rithms. The resulting resolution for positrons was 2 mrad for $\theta_e < 23°$, 3 mrad for $23° < \theta_e < 156°$ and 5 mrad for $\theta_e > 156°$.

VII. RECONSTRUCTION OF THE HADRONIC SYSTEM

A. Hadronic-energy determination

The hadronic-energy deposits were corrected for energy loss in the material between the interaction point and the calorimeter using the material maps implemented in the detector-simulation package. After applying all corrections, the measured resolution for the transverse momentum of the hadronic final state, $P_{T,h}$, was about 13% (11%) at $P_{T,h} = 20$ GeV in BCAL (FCAL), decreasing to 8% (7.5%) at $P_{T,h} = 60$ GeV. The uncertainties in the hadronic-energy scales of the FCAL and the BCAL were ±1%, while for the RCAL the uncertainty was ±2% [35].

B. Determination of the hadronic polar angle γ_h

The angle γ_h is given by [29]

$$\cos\gamma_h = \frac{P_{T,h}^2 - \delta_h^2}{P_{T,h}^2 + \delta_h^2},$$

where $P_{T,h}$ and δ_h were calculated from Eqs. (2) and (3) using only the hadronic energy. Particles scattered by interactions in the material between the primary vertex and the CAL generate energy deposits in the CAL that bias the reconstructed value of γ_h. To minimize this bias, an algorithm was developed in which CAL clusters with energies below 3 GeV and with polar angles larger than an angle γ_{max} were removed [1]. The value of γ_{max} was derived from a NC MC sample by minimizing the bias in the reconstructed hadronic variables.

The resolution of γ_h is below 15 mrad for $\gamma_h < 0.2$ rad, increasing to 100 mrad at $\gamma_h \approx 2$ rad. These resolutions dominate the uncertainties on the kinematic variables.

VIII. EVENT SELECTION

A. Trigger

ZEUS operates a three-level trigger system [12,36]. At the first-level trigger, only coarse calorimeter and tracking information is available. Events were selected using criteria based on an energy deposit in the CAL consistent with an isolated positron. In addition, events with high E_T in coincidence with a CTD track were accepted. At the second level, a requirement on δ was used to select NC DIS events and timing information from the calorimeter was used to reject events inconsistent with the bunch-crossing time. At the third level, events were fully reconstructed on a computer farm. The requirements were similar to, but looser than, the offline cuts described

below; a simpler and generally more efficient (but less pure) positron finder was used.

The main uncertainty in the trigger efficiency comes from the first level. The data and MC simulation agree to within ~0.5% and the overall efficiency is close to 100% [27].

B. Offline selection

The following criteria were applied offline:

  (i) positrons, identified as described in Sec. VI, were required to satisfy the following criteria:

    (1) to reduce background, isolated positrons were selected by requiring that less than 5GeV be deposited in calorimeter cells not associated with the scattered positron, inside an η-ϕ cone of radius $R_{cone} = 0.8$ centered on the positron. For those positrons with a matched track, the momentum of the track, $p$trk, was required to be at least 5GeV. For positrons outside the forward tracking acceptance of the CTD, the tracking requirement in the positron selection was replaced by a cut on the transverse-momentum of the positron, $p_T^e > 30$GeV. For positrons outside the backward tracking acceptance of the CTD, no track was required;

    (2) a fiducial-volume cut was applied to the positron to guarantee that the experimental acceptance was well understood. It excluded the upper part of the central RCAL area occluded by the cryogenic supply for the solenoid magnet as well as the transition regions between the three parts of the CAL [37,38];

  (ii) to ensure that event quantities were accurately determined, a reconstructed vertex with $-50 < Z < 50$ cm was required, a range consistent with the ep interaction region. A small fraction of the proton-beam current was contained in satellite bunches, which were shifted by ± 4.8 ns with respect to the nominal bunch-crossing time, resulting in a few of the ep interactions occurring ± 72 cm from the nominal interaction point. This cut rejects ep events from these regions;

  (iii) to suppress photoproduction events, in which the scattered positron escaped through the beam hole in the RCAL, δ was required to be greater than 38 GeV. This cut also rejected events with large initial-state QED radiation. The requirement $\delta < 65$ GeV removed "overlay" events in which a normal DIS event coincided with additional energy deposits in the RCAL from some other reaction. This requirement had a negligible effect on the efficiency for selecting NC DIS events. For positrons outside the forward tracking acceptance of the CTD, the lower δ cut was raised to 44 GeV;

  (iv) to further reduce background from photoproduction events, y_e was required to satisfy $y_e < 0.95$;

  (v) the net transverse momentum, P_T, is expected to be close to zero for true NC events and was measured with an uncertainty approximately proportional to $\sqrt{E_T}$. To remove cosmic rays and beam-related backgrounds, $P_T/\sqrt{E_T}$ was required to be less than $4\sqrt{GeV}$;

  (vi) to reduce the size of the QED radiative corrections, elastic Compton scattering events ($ep \rightarrow e\gamma p$) were removed. This was done using an algorithm that searched for an additional photon candidate and discarded the event if the sum of the energies associated with the positron and photon candidates was within 2 GeV of the total energy measured in the calorimeter. The contribution from deeply virtual Compton scattering was estimated to be negligible;

  (vii) in events with low γ_h, a large amount of energy is deposited near the inner edges of the FCAL or escapes through the forward beam pipe. As the MC simulation of the very forward energy flow is problematic [37], events where γ_h, extrapolated to the FCAL surface, lay within a circle of radius 20 cm around the forward beam line were removed. For an interaction at the nominal interaction point, this FCAL circle cut corresponds to a lower γ_h cut of 90 mrad. This cut rejects events at very low y that have high x;

  (viii) the kinematic range over which the MC generator is valid does not extend to very low y at high x. To avoid these regions of phase space, in addition to the previous cut, $y_{JB}(1 - x_{DA})^2$ was required to be greater than 0.004 [39].

A total of 156 962 events with $Q_{DA}^2 > 185$ GeV^2 satisfied the above criteria. Data distributions are compared to the sum of the signal and photoproduction MC samples in Fig. 1. The signal MC includes a diffractive component, as discussed in Sec. IV. Good agreement between data and MC simulation is seen over the full range of most variables. Imperfections in the MC simulation can be seen in the disagreement between data and MC simulation that occurs in the region of the kinematic peak ($E_e' \approx E_e$) in the positron-energy distribution, and correspondingly in the peak region of the δ distribution. The effect of these differences on the cross-section measurements is evaluated in the systematic uncertainties assigned to the positron-energy scale and to the positron-energy resolution (see Sec. IX B).

The photoproduction background was <0.3% over most of the kinematic range covered, rising to ~1.7% at high y. From the study of empty positron and proton
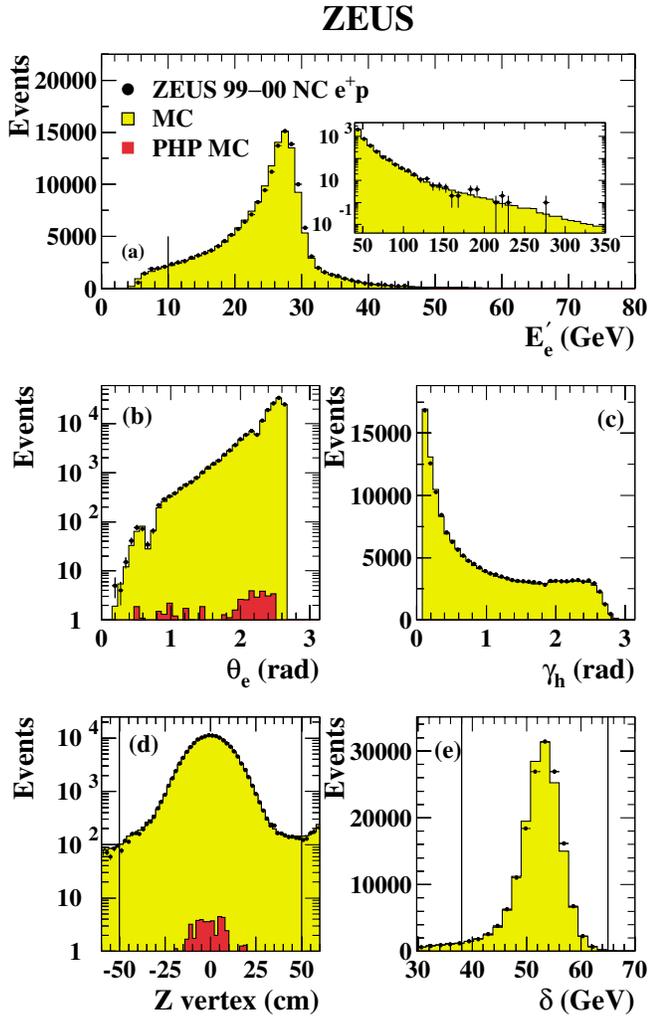
ZEUS

FIG. 1 (color online). Comparison of e^+p data (points) and MC simulation (histograms) for: (a) the energy of the scattered positron, E'_e (the inset shows the high-energy part of the distribution); (b) the angle of the scattered positron, θ_e; (c) the hadronic angle, γ_h; (d) the Z coordinate of the event vertex; (e) the δ variable. The vertical lines indicate the cut boundaries described in the text. The darker histogram visible in the θ_e and Z vertex figures corresponds to the photoproduction background.

buckets, it was concluded that possible backgrounds associated with non-ep collisions could be neglected.

IX. RESULTS

A. Binning, acceptance and cross-section determination

The bin sizes used for the determination of the single- and double-differential cross sections were chosen commensurate with the resolutions. Figure 2 shows the kinematic region used in extracting the e^+p double-differential cross section. The number of events per bin decreases from ~7000 in the lowest-Q^2 bins to five in the

ZEUS
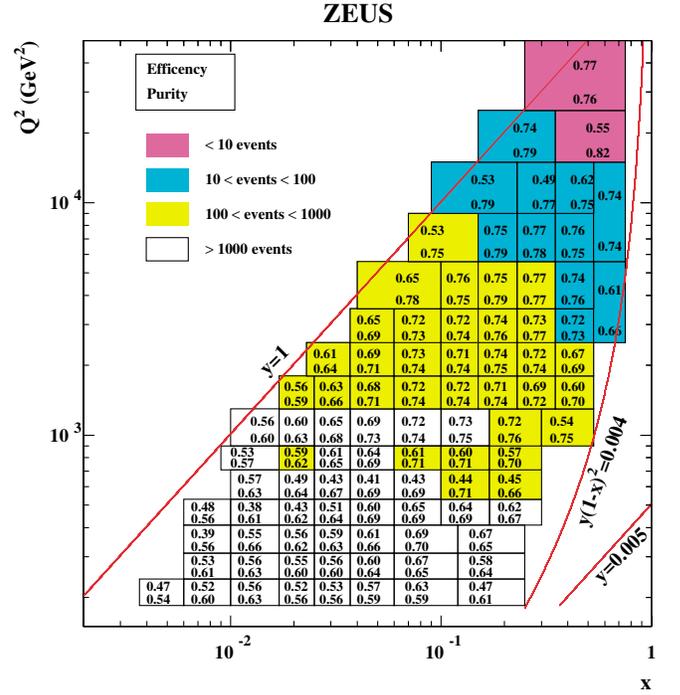
FIG. 2 (color online). Bins used in the extraction of the double-differential cross section. The solid diagonal lines are isolines of y drawn for $y = 1$ (the kinematic limit) and $y = 0.005$. The curved line indicates the cut on $y_{JB}(1 - x_{DA})^2$ described in Sec. VIII B. An indication of the approximate number of events from the final sample that lie in each bin is given by the shading level. The efficiency and purity for each bin is shown.

bin at the highest Q^2 and x. The efficiency after all selection cuts (defined as the number of events generated and reconstructed in a bin after all selection cuts divided by the number of events that were generated in that bin) varied between 50% and 80%. In some medium-Q^2 bins, dominated by events in which the positron is scattered into the region between the R/BCAL at $\theta_e \sim 2.25$ rad, the efficiency decreases to around 40%. The purity (defined as the number of events reconstructed and generated in a bin after all selection cuts divided by the total number of events reconstructed in that bin) ranged from 50% to 80%. The efficiency and purity in double-differential bins are shown in Fig. 2.

The value of the cross section in a particular bin, for example, for $d^2\sigma/dxdQ^2$, was determined according to

$$\frac{d^2\sigma}{dxdQ^2} = \frac{N_{\text{data}} - N_{\text{bg}}}{N_{\text{MC}}} \cdot \frac{d^2\sigma_{\text{Born}}^{\text{SM}}}{dxdQ^2},$$

where N_{data} is the number of data events in the bin, N_{bg} is the number of background events estimated from the photoproduction MC and N_{MC} is the number of signal MC events normalized to the luminosity of the data. The SM prediction, $d^2\sigma_{\text{Born}}^{\text{SM}}/dxdQ^2$, was evaluated according to Eq. (1) using CTEQ5D PDFs [20] and using the

ZEUS

(a) The differential $e^{\pm}p$ cross section $d\sigma/dQ^2$ compared to the Standard Model expectation evaluated using the ZEUS-S PDFs.

Legend:
- ● ZEUS 99–00 NC e^+p
- □ ZEUS 98–99 NC e^-p
- —— ZEUS-S e^+p
- ----- ZEUS-S e^-p

(b) $Q^2 > 10000$ GeV^2

FIG. 3 (color online).   (a) The differential $e^{\pm}p$ cross section $d\sigma/dQ^2$ compared to the Standard Model expectation evaluated using the ZEUS-S PDFs. (b) The differential e^+p cross section $d\sigma/dx$ for $Q^2 > 10\,000$ GeV^2 as a function of x. The inner bars show the statistical uncertainty, while the outer ones show the statistical and systematic uncertainties added in quadrature.

TABLE I.   The single-differential cross section $d\sigma/dQ^2$ for the reaction $e^+p \rightarrow e^+X$. The following quantities are given for each bin: the Q^2 range, the value at which the cross section is quoted, Q_c^2, and the measured cross section $d\sigma/dQ^2$ corrected to the electroweak Born level. The first uncertainty on the measured cross section is the statistical uncertainty and the second is the systematic uncertainty. The uncertainty on the measured luminosity of 2.5% is not included in the total systematic uncertainty.

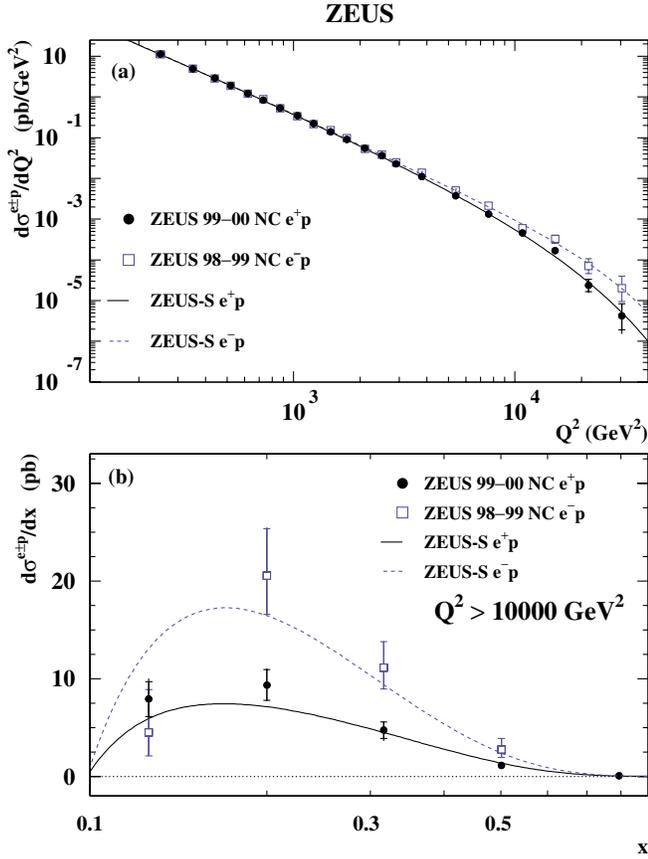| Q^2 range (GeV^2)	Q_c^2 (GeV^2)	$d\sigma/dQ^2$ (pb/GeV^2)
200.0–300.0	250	$11.310 \pm 0.055^{+0.107}_{-0.097}$
300.0–400.0	350	$4.932 \pm 0.037^{+0.063}_{-0.045}$
400.0–475.7	440	$2.880 \pm 0.031^{+0.038}_{-0.019}$
475.7–565.7	520	$1.917 \pm 0.024^{+0.031}_{-0.018}$
565.7–672.7	620	$1.225 \pm 0.018^{+0.024}_{-0.015}$
672.7–800.0	730	$(8.39 \pm 0.13^{+0.12}_{-0.08}) \times 10^{-1}$
800.0–951.4	870	$(5.38 \pm 0.09^{+0.06}_{-0.04}) \times 10^{-1}$
951.4–1131.0	1040	$(3.47 \pm 0.06^{+0.05}_{-0.03}) \times 10^{-1}$
1131.0–1345.0	1230	$(2.24 \pm 0.05^{+0.03}_{-0.03}) \times 10^{-1}$
1345.0–1600.0	1470	$(1.39 \pm 0.03^{+0.02}_{-0.01}) \times 10^{-1}$
1600.0–1903.0	1740	$(9.15 \pm 0.23^{+0.13}_{-0.16}) \times 10^{-2}$
1903.0–2263.0	2100	$(5.46 \pm 0.16^{+0.06}_{-0.06}) \times 10^{-2}$
2263.0–2691.0	2500	$(3.64 \pm 0.12^{+0.04}_{-0.06}) \times 10^{-2}$
2691.0–3200.0	2900	$(2.30 \pm 0.09^{+0.06}_{-0.03}) \times 10^{-2}$
3200.0–4525.0	3800	$(1.11 \pm 0.04^{+0.01}_{-0.02}) \times 10^{-2}$
4525.0–6400.0	5400	$(3.76 \pm 0.18^{+0.07}_{-0.05}) \times 10^{-3}$
6400.0–9051.0	7600	$(1.33 \pm 0.10^{+0.02}_{-0.05}) \times 10^{-3}$
9051.0–12 800.0	10 800	$(4.55 \pm 0.51^{+0.16}_{-0.18}) \times 10^{-4}$
12 800.0–18 100.0	15 200	$(1.65 \pm 0.27^{+0.04}_{-0.13}) \times 10^{-4}$
18 100.0–25 600.0	21 500	$(2.35^{+0.94+0.31}_{-0.70-0.41}) \times 10^{-5}$
25 600.0–36 200.0	30 400	$(4.2^{+4.1+0.3}_{-2.3-1.4}) \times 10^{-6}$

Particle Data Group values [21] for the fine-structure constant, the mass of the Z boson and the weak mixing angle. This procedure implicitly takes the acceptance, bin-centering and radiative corrections from the MC simulation. A similar procedure was used for $d\sigma/dx$, $d\sigma/dy$ and $d\sigma/dQ^2$. In this way, the cross sections $d\sigma/dx$ and $d\sigma/dQ^2$ were extrapolated to the full y range.

The statistical uncertainties on the cross sections were calculated from the numbers of events observed in the bins, taking into account the statistical uncertainty from the MC simulation (signal and background). Poisson statistics were used for all bins.

B. Systematic uncertainties

Systematic uncertainties associated with the MC simulation were estimated by recalculating the cross section after modifying the simulation to account for known uncertainties. Cut values were varied where this method was not applicable. The positive and negative deviations from the nominal cross-section values were added in quadrature separately to obtain the total positive and negative systematic uncertainty. The uncertainty on the luminosity of the combined 1999/2000 e^+p sample is 2.5% and was not included in the total systematic uncertainty. The other uncertainties are discussed in detail below.

1. Uncorrelated systematic uncertainties

The following systematic uncertainties are either small or exhibit no bin-to-bin correlations:

(i) positron-energy resolution in the MC simulation: the effect on the cross sections of changing the CAL energy resolution for the scattered positron in the MC by $\pm 1\%$ was negligible over almost the full kinematic range. The effect increased to $\sim \pm 1\%$ only for $d\sigma/dy$ bins at high y and for double-differential bins at high Q^2;

TABLE II. Systematic uncertainties with bin-to-bin correlations for the single-differential cross section $d\sigma/dQ^2$. The left part of the table contains the value at which the cross section is quoted, Q_c^2, the measured cross section $d\sigma/dQ^2$ corrected to the electroweak Born level, the statistical uncertainty and the total systematic uncertainty. The uncertainty on the measured luminosity of 2.5% is not included in the total systematic uncertainty. The right part of the table lists the total uncorrelated systematic uncertainty followed by the bin-to-bin correlated systematic uncertainties $\delta_1 - \delta_8$ defined in the text. For the latter, the upper (lower) numbers refer to positive (negative) variation of, e.g., the cut value, whereas the signs of the numbers reflect the direction of change in the cross sections.

Q_c^2 (GeV²)	$d\sigma/dQ^2$ (pb/GeV²)	Stat. (%)	Total sys. (%)	Uncor. sys. (%)	δ_1 (%)	δ_2 (%)	δ_3 (%)	δ_4 (%)	δ_5 (%)	δ_6 (%)	δ_7 (%)	δ_8 (%)
250	11.310	$^{+0.5}_{-0.5}$	$^{+0.9}_{-0.9}$	$^{+0.1}_{-0.3}$	$^{-0.4}_{+0.4}$	$+0.0$	$^{-0.0}_{-0.0}$	$^{-0.6}_{+0.7}$	$^{-0.3}_{+0.3}$	$^{+0.2}_{-0.5}$	$+0.1$	$^{+0.0}_{-0.0}$
350	4.932	$^{+0.7}_{-0.7}$	$^{+1.3}_{-0.9}$	$^{+0.2}_{-0.2}$	$^{-0.4}_{+0.4}$	$+0.0$	$^{+0.0}_{+0.0}$	$^{-0.7}_{+1.1}$	$^{-0.3}_{+0.3}$	$^{+0.1}_{-0.2}$	$+0.2$	$^{+0.1}_{-0.1}$
440	2.880	$^{+1.1}_{-1.1}$	$^{+1.3}_{-0.6}$	$^{+0.5}_{-0.3}$	$^{-0.4}_{+0.4}$	$+0.0$	$^{-0.0}_{+0.0}$	$^{-0.2}_{+1.1}$	$^{-0.3}_{+0.3}$	$^{+0.1}_{-0.2}$	-0.0	$^{+0.1}_{-0.1}$
520	1.917	$^{+1.2}_{-1.2}$	$^{+1.6}_{-0.9}$	$^{+0.4}_{-0.6}$	$^{-0.4}_{+0.4}$	-0.0	$^{+0.0}_{-0.0}$	$^{-0.5}_{+1.4}$	$^{-0.3}_{+0.3}$	$^{+0.2}_{-0.4}$	$+0.5$	$^{+0.0}_{-0.0}$
620	1.225	$^{+1.5}_{-1.5}$	$^{+1.9}_{-1.2}$	$^{+0.3}_{-0.5}$	$^{-0.4}_{+0.4}$	$+0.1$	$^{-0.0}_{+0.0}$	$^{-0.5}_{+1.9}$	$^{-0.2}_{+0.2}$	$^{+0.1}_{-0.2}$	-0.9	$^{-0.0}_{+0.0}$
730	8.393×10^{-1}	$^{+1.5}_{-1.5}$	$^{+1.4}_{-0.9}$	$^{+0.4}_{-0.4}$	$^{-0.3}_{+0.3}$	$+0.0$	$^{+0.1}_{+0.1}$	$^{-0.7}_{+1.1}$	$^{-0.3}_{+0.3}$	$^{+0.2}_{-0.5}$	$+0.5$	$^{+0.0}_{-0.1}$
870	5.377×10^{-1}	$^{+1.6}_{-1.6}$	$^{+1.1}_{-0.8}$	$^{+0.6}_{-0.5}$	$^{-0.2}_{+0.3}$	-0.2	$^{-0.0}_{+0.1}$	$^{-0.0}_{+0.7}$	$^{-0.4}_{+0.4}$	$^{+0.1}_{-0.2}$	-0.3	$^{+0.1}_{-0.1}$
1040	3.474×10^{-1}	$^{+1.8}_{-1.8}$	$^{+1.4}_{-0.9}$	$^{+0.2}_{-0.5}$	$^{-0.2}_{+0.2}$	-0.0	$^{+0.0}_{-0.2}$	$^{-0.6}_{+1.3}$	$^{-0.3}_{+0.3}$	$^{+0.1}_{-0.3}$	$+0.0$	$^{+0.1}_{-0.1}$
1230	2.238×10^{-1}	$^{+2.0}_{-2.0}$	$^{+1.5}_{-1.2}$	$^{+0.4}_{-0.5}$	$^{-0.1}_{+0.2}$	-0.5	$^{+0.1}_{+0.1}$	$^{-0.8}_{+1.4}$	$^{-0.3}_{+0.3}$	$^{+0.0}_{-0.1}$	$+0.2$	$^{+0.1}_{-0.1}$
1470	1.394×10^{-1}	$^{+2.2}_{-2.2}$	$^{+1.5}_{-0.9}$	$^{+0.6}_{-0.5}$	$^{-0.1}_{+0.2}$	$+0.1$	$^{-0.1}_{-0.1}$	$^{-0.6}_{+1.1}$	$^{-0.4}_{+0.3}$	$^{+0.0}_{-0.1}$	$+0.6$	$^{+0.1}_{-0.1}$
1740	9.154×10^{-2}	$^{+2.5}_{-2.5}$	$^{+1.4}_{-1.8}$	$^{+0.6}_{-0.7}$	$^{-0.1}_{+0.1}$	$+0.2$	$^{-0.0}_{+0.1}$	$^{-0.1}_{+1.2}$	$^{-0.4}_{+0.4}$	$^{+0.2}_{-0.5}$	-1.5	$^{+0.1}_{-0.1}$
2100	5.458×10^{-2}	$^{+2.9}_{-2.9}$	$^{+1.1}_{-1.1}$	$^{+0.5}_{-0.8}$	$^{-0.1}_{+0.2}$	$+0.5$	$^{+0.1}_{+0.0}$	$^{-0.2}_{+0.5}$	$^{-0.3}_{+0.3}$	$^{+0.2}_{-0.4}$	-0.5	$^{+0.1}_{-0.1}$
2500	3.635×10^{-2}	$^{+3.3}_{-3.3}$	$^{+1.1}_{-1.6}$	$^{+0.5}_{-0.7}$	$^{-0.1}_{+0.2}$	$+0.5$	$^{-0.1}_{+0.1}$	$^{+0.3}_{+0.6}$	$^{-0.3}_{+0.3}$	$^{+0.4}_{-1.0}$	-1.0	$^{+0.1}_{-0.1}$
2900	2.298×10^{-2}	$^{+3.8}_{-3.8}$	$^{+2.5}_{-1.3}$	$^{+1.2}_{-1.0}$	$^{-0.1}_{+0.2}$	-0.3	$^{+0.1}_{+0.2}$	$^{-0.6}_{+0.8}$	$^{-0.3}_{+0.3}$	$^{+0.3}_{-0.8}$	$+1.7$	$^{+0.1}_{-0.1}$
3800	1.113×10^{-2}	$^{+3.4}_{-3.4}$	$^{+0.5}_{-1.8}$	$^{+0.4}_{-0.9}$	$^{-0.1}_{+0.2}$	-1.0	$^{-0.0}_{-0.1}$	$^{+0.0}_{-0.3}$	$^{-0.3}_{+0.3}$	$^{+0.0}_{-0.0}$	-1.0	$^{+0.0}_{-0.0}$
5400	3.756×10^{-3}	$^{+4.8}_{-4.8}$	$^{+2.0}_{-1.3}$	$^{+1.3}_{-0.5}$	$^{-0.1}_{+0.1}$	-1.0	$^{-0.1}_{-0.5}$	$^{+0.2}_{+0.3}$	$^{-0.4}_{+0.4}$	$^{+0.3}_{-0.6}$	$+1.2$	$^{-0.0}_{+0.0}$
7600	1.331×10^{-3}	$^{+7.2}_{-7.2}$	$^{+1.3}_{-3.4}$	$^{+0.6}_{-2.2}$	$^{-0.3}_{+0.2}$	-1.0	$^{-0.3}_{-0.1}$	$^{+0.9}_{+0.4}$	$^{-0.4}_{+0.4}$	$^{+0.2}_{-0.5}$	-2.3	$^{-0.0}_{+0.0}$
10 800	4.551×10^{-4}	$^{+11.0}_{-11.0}$	$^{+3.4}_{-3.9}$	$^{+2.8}_{-2.6}$	$^{-0.4}_{+0.5}$	-1.0	$^{-0.9}_{-2.3}$	$^{-0.9}_{+0.8}$	$^{-0.4}_{+0.4}$	$^{+0.1}_{-0.3}$	$+1.8$	$^{+0.1}_{-0.1}$
15 200	1.655×10^{-4}	$^{+16.0}_{-16.0}$	$^{+2.1}_{-8.1}$	$^{+0.4}_{-7.9}$	$^{-0.3}_{+0.6}$	-1.0	$^{-1.0}_{+0.5}$	$^{+1.9}_{-0.5}$	$^{-0.3}_{+0.3}$	$^{+0.2}_{-0.4}$	-0.0	$^{-0.1}_{+0.0}$
21 500	2.353×10^{-5}	$^{+40.0}_{-30.0}$	$^{+13.0}_{-18.0}$	$^{+9.6}_{-9.0}$	$^{-0.5}_{+0.4}$	-1.0	$^{-1.1}_{-15.0}$	$^{+3.0}_{+8.2}$	$^{-0.4}_{+0.4}$	$^{+0.5}_{-1.1}$	$+0.9$	$^{+0.2}_{-0.2}$
30 400	4.217×10^{-6}	$^{+97.0}_{-54.0}$	$^{+6.5}_{-33.}$	$^{+4.2}_{-33.0}$	$^{-0.7}_{+0.3}$	-1.0	$^{-1.1}_{+3.7}$	$^{+2.4}_{-0.5}$	$^{-0.4}_{+0.4}$	$^{+0.9}_{-2.0}$	$+0.5$	$^{+0.4}_{-0.5}$

(ii) positron angle: differences between data and MC simulation in the positron scattering angle due to uncertainties in the simulation of the CTD were at most 1 mrad. Typically, the deviations were within $\pm 1\%$; the effect increased to as much as $\pm 2\%$ only in a few high-Q^2 double-differential bins, but was small compared to the statistical uncertainty;

(iii) hadronic angle: the uncertainty associated with the reconstruction of γ_h was investigated by varying the calorimeter energy scale for the hadronic final state separately for R/B/FCAL as described in Sec. VII A and by varying γ_{max} in a range for which the reconstructed value of γ_h remained close to optimal. This resulted in an estimated systematic uncertainty in the single-differential cross sections of less than $\pm 1\%$ in most bins, increasing to $\sim \pm 5\%$ in a few high-Q^2 bins. For $d^2\sigma/dxdQ^2$, the effect is generally below $\pm 2\%$ at low and medium Q^2, but is relevant at low Q^2 and

low y due to the small statistical uncertainty in this region;

(iv) FCAL circle cut: the FCAL circle cut at 20 cm was varied by ± 3 cm. The resulting changes in the cross sections were typically below $\pm 1\%$. Only for the highest x bins of the double-differential cross section did the effect increase to $\pm 4\%$;

(v) background estimation:

    (1) systematic uncertainties arising from the normalization of the photoproduction background were estimated by changing the background normalization by a factor of $\pm 40\%$, resulting in negligible changes in the single-differential cross sections over the full kinematic range and variations of less than $\pm 1\%$ in the double-differential bins;

    (2) the cut on the distance of closest approach between the extrapolated positron track and
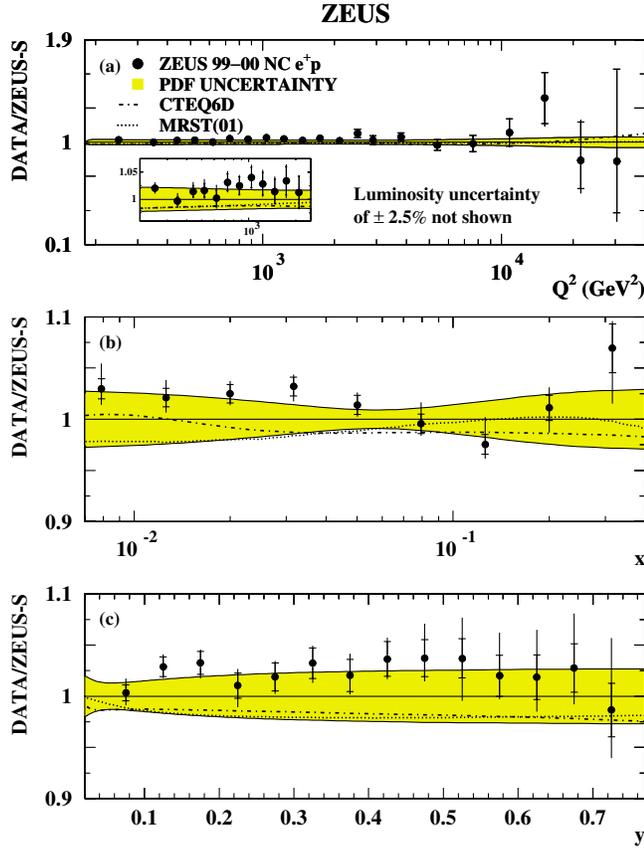
ZEUS

FIG. 4 (color online). Ratios of the single-differential e^+p cross sections to the Standard Model expectation evaluated using the ZEUS-S PDFs: (a) $d\sigma/dQ^2$ (the inset shows the low Q^2 region); (b) $d\sigma/dx$ for $Q^2 > 200$ GeV^2; (c) $d\sigma/dy$ for $Q^2 > 200$ GeV^2. The shaded band indicates the uncertainty on the calculated cross sections due to the uncertainty in the ZEUS-S PDFs. The inner bars show the statistical uncertainty, while the outer ones show the statistical and systematic uncertainties added in quadrature. The results obtained using the CTEQ6D and the MRST(01) PDFs are shown as the dash-dotted and dotted lines, respectively.

the calorimeter cluster associated with the positron was changed to 8 cm to estimate the background contamination from wrongly identified positrons. The uncertainties in the cross sections associated with this variation were below $\pm 1\%$ over the full kinematic range and small compared to the statistical uncertainty;

(3) the uncertainty due to overlay events, in which a normal DIS event coincided with additional energy deposits in the RCAL from some other interaction, was estimated by narrowing or widening the 38 GeV $< \delta < 65$ GeV interval symmetrically by ± 4 GeV. The effect on the cross sections was typically below 1%; in a few high-Q^2

double-differential bins, the uncertainty was as large as 6% but nevertheless small compared to the statistical uncertainty;

(4) the systematic uncertainty associated with the cosmic-ray rejection was evaluated by varying the $P_T/\sqrt{E_T}$ cut by $\pm 1\sqrt{\text{GeV}}$. The cross-section uncertainties were below $\pm 1\%$ over the full kinematic range;

(vi) diffractive contribution: the fraction of diffractive events was varied within the uncertainty determined from the fit described in Sec. IV. The resulting uncertainties were typically below $\pm 1\%$.

The positron identification efficiency was checked with a data sample of NC DIS events selected using independent requirements [40]. The efficiency curves from data and MC simulation agreed to better than 0.5%. An alternative positron-finding algorithm [4] was also used: differences in the measured cross sections were less than 0.5%. Systematic uncertainties from both of these effects were neglected.

2. Correlated systematic uncertainties

The following systematic uncertainties were correlated bin-to-bin:

(i) $\{\delta_1\}$ positron energy scale: the uncertainty in the positron energy scale (as described in Sec. VI) resulted in systematic variations in the $d\sigma/dy$ cross section that were comparable to the statistical uncertainty at high y and small elsewhere;

(ii) $\{\delta_2\}$ background estimation: systematic uncertainties arising from the estimation of the photoproduction background were also estimated by reducing the cut on y_e to $y_e < 0.9$. The resulting changes in the cross sections were typically below $\pm 2\%$. In the highest-Q^2 region at low x, where the statistics were low, an average uncertainty of -0.3% was estimated;

(iii) $\{\delta_3\}$ variation of selection cuts (I): varying the positron isolation requirement by ± 2 GeV caused a small systematic uncertainty in the cross sections at the lower end of the Q^2 range and up to $\pm 4\%$ in the highest-Q^2 region, where it was still small compared to the statistical uncertainty;

(iv) $\{\delta_4\}$ variation of selection cuts (II): the MC description of the positron momentum as measured from the positron track, p_{trk}, was not perfect. Varying the p_{trk} requirement by ± 5 GeV resulted in a variation of the cross section of the order $\pm 2\%$ over most of the kinematic range. The effect was comparable to the statistical uncertainty in a few double-differential bins at low x and low Q^2 and in low-x or high-y bins in the single-differential cross sections;

TABLE III. The single-differential cross section $d\sigma/dx$ for the reaction $e^+p \to e^+X$. The following quantities are given for each bin: the lower Q^2 cut, the x range, the value at which the cross section is quoted, x_c, and the measured cross section $d\sigma/dx$ corrected to the electroweak Born level. The first uncertainty on the measured cross section is the statistical uncertainty and the second is the systematic uncertainty. The uncertainty on the measured luminosity of 2.5% is not included in the total systematic uncertainty.

Q^2 cut (GeV²)	x range	x_c	$d\sigma/dx$ (pb)
200	$(0.63\text{–}1.00) \times 10^{-2}$	0.790×10^{-2}	$(8.13 \pm 0.08^{+0.18}_{-0.10}) \times 10^4$
	$(0.10\text{–}0.16) \times 10^{-1}$	0.126×10^{-1}	$(5.42 \pm 0.05^{+0.08}_{-0.06}) \times 10^4$
	$(0.16\text{–}0.25) \times 10^{-1}$	0.200×10^{-1}	$(3.38 \pm 0.03^{+0.03}_{-0.02}) \times 10^4$
	$(0.25\text{–}0.40) \times 10^{-1}$	0.316×10^{-1}	$(2.03 \pm 0.02^{+0.01}_{-0.02}) \times 10^4$
	$(0.40\text{–}0.63) \times 10^{-1}$	0.501×10^{-1}	$(1.15 \pm 0.01^{+0.01}_{-0.01}) \times 10^4$
	$(0.63\text{–}1.00) \times 10^{-1}$	0.794×10^{-1}	$(6.44 \pm 0.06^{+0.12}_{-0.05}) \times 10^3$
	$0.10\text{–}0.16$	0.126	$(3.49 \pm 0.03^{+0.09}_{-0.04}) \times 10^3$
	$0.16\text{–}0.25$	0.200	$(1.87 \pm 0.02^{+0.03}_{-0.04}) \times 10^3$
	$0.25\text{–}0.40$	0.316	$(8.47 \pm 0.19^{+0.09}_{-0.38}) \times 10^2$
10 000	$0.10\text{–}0.16$	0.126	$7.91 \pm 1.78^{+1.15}_{-0.95}$
	$0.16\text{–}0.25$	0.200	$9.35 \pm 1.57^{+0.66}_{-0.34}$
	$0.25\text{–}0.40$	0.316	$4.72 \pm 0.84^{+0.25}_{-0.74}$
	$0.40\text{–}0.63$	0.501	$1.13 \pm 0.31^{+0.05}_{-0.14}$
	$0.63\text{–}1.00$	0.794	$0.05^{+0.06+0.00}_{-0.03-0.03}$

(v) $\{\delta_5\}$ vertex distribution: the uncertainty in the cross sections arising from the measurement of the shape of the distribution of the Z coordinate of the event vertex was obtained by varying the contribution of events from the satellite bunches, visible as small peaks at $|Z| > 50$ cm in Fig. 1(d), within their uncertainties in the MC simulation. The effect on the cross sections was

TABLE IV. Systematic uncertainties with bin-to-bin correlations for the single-differential cross section $d\sigma/dx$. The left part of the table contains the lower Q^2 cut, the value at which the cross section is quoted, x_c, the measured cross section $d\sigma/dx$ corrected to the electroweak Born level, the statistical uncertainty, and the total systematic uncertainty. The uncertainty on the measured luminosity of 2.5% is not included in the total systematic uncertainty. The right part of the table lists the total uncorrelated systematic uncertainty followed by the bin-to-bin correlated systematic uncertainties δ_1–δ_8 defined in the text. For the latter, the upper (lower) numbers refer to positive (negative) variation of, e.g., the cut value, whereas the signs of the numbers reflect the direction of change in the cross sections.

Q^2 cut (GeV²)	x_c	$d\sigma/dx$ (pb)	Stat. (%)	Total sys. (%)	Uncor. sys. (%)	δ_1 (%)	δ_2 (%)	δ_3 (%)	δ_4 (%)	δ_5 (%)	δ_6 (%)	δ_7 (%)	δ_8 (%)
200	0.790×10^{-2}	8.13×10^4	+0.9 / −0.9	+2.2 / −1.2	+0.7 / −0.2	−0.4 / +0.4	+0.0	+0.0 / +0.1	−0.9 / +2.1	−0.3 / +0.3	+0.1 / −0.2	−0.2	+0.0 / −0.0
	0.126×10^{-1}	5.42×10^4	+0.9 / −0.9	+1.5 / −1.1	+0.5 / −0.2	−0.1 / +0.2	−0.1	−0.0 / −0.0	−0.8 / +1.3	−0.3 / +0.3	+0.3 / −0.6	+0.3	−0.0 / +0.0
	0.200×10^{-1}	3.38×10^4	+0.9 / −0.9	+0.8 / −0.7	+0.4 / −0.2	−0.2 / +0.1	+0.1	+0.0 / +0.0	−0.2 / +0.6	−0.3 / +0.3	+0.1 / −0.3	−0.1	−0.1 / +0.1
	0.316×10^{-1}	2.03×10^4	+0.9 / −0.9	+0.7 / −1.1	+0.4 / −0.3	−0.1 / +0.2	−0.0	+0.0 / +0.0	−0.6 / +0.2	−0.3 / +0.3	+0.2 / −0.4	−0.8	−0.2 / +0.2
	$0.501- \times 10^{-1}$	1.15×10^4	+0.9 / −0.9	+0.7 / −0.7	+0.6 / −0.1	−0.1 / +0.2	−0.0	+0.0 / +0.0	−0.3 / +0.3	−0.3 / +0.3	+0.0 / −0.1	+0.2	−0.3 / +0.3
	0.794×10^{-1}	6.44×10^3	+0.9 / −0.9	+1.9 / −0.7	+0.3 / −0.2	−0.2 / +0.2	−0.0	−0.0 / −0.0	−0.1 / +0.4	−0.3 / +0.3	+0.5 / −1.1	+1.3	−0.2 / +0.2
	0.126	3.49×10^3	+1.0 / −1.0	+2.5 / −1.0	+0.3 / −0.4	−0.2 / +0.2	+0.0	−0.0 / −0.0	−0.3 / +0.7	−0.3 / +0.3	+0.8 / −1.9	+1.5	+0.0 / +0.0
	0.200	1.87×10^3	+1.2 / −1.2	+1.6 / −2.0	+0.6 / −1.5	−0.2 / +0.2	+0.0	−0.0 / −0.0	−0.4 / +0.0	−0.4 / +0.4	+0.6 / −1.4	−1.0	+0.3 / −0.3
	0.316	8.47×10^2	+2.2 / −2.2	+1.1 / −4.5	+0.5 / −2.3	−0.2 / +0.2	−0.2	−0.0 / −0.1	+0.1 / +0.0	−0.4 / +0.4	+0.3 / −0.8	−3.8	+0.3 / −0.4
10 000	0.126	7.91	+23.0 / −23.0	+14.0 / −12.0	+4.5 / −9.4	−0.9 / +1.7	+13.	−3.1 / −5.9	+3.0 / −1.0	−0.4 / +0.4	+1.3 / −3.1	−0.6	−0.2 / +0.2
	0.200	9.35	+17.0 / −17.0	+7.1 / −3.6	+0.8 / −3.4	−0.2 / +0.2	+3.1	−1.1 / +0.3	+2.1 / −0.5	−0.3 / +0.3	+0.2 / −0.5	+6.0	−0.1 / +0.1
	0.316	4.72	+18.0 / −18.0	+5.3 / −16.0	+4.3 / −3.7	−0.3 / +0.3	−14.	−0.6 / −4.7	+1.6 / +2.6	−0.4 / +0.4	+0.1 / −0.3	−3.3	−0.0 / +0.0
	0.501	1.13	+28.0 / −28.0	+4.6 / −12.0	+3.5 / −10.0	−0.2 / +0.3	+0.6	−0.4 / +1.3	−6.4 / −0.3	−0.4 / +0.4	+0.2 / −0.4	+2.6	−0.1 / +0.1
	0.794	0.05	+132.0 / −65.0	+7.3 / −67.0	+4.9 / −47.0	−0.3 / +0.6	+0.2	−0.1 / +1.1	+0.7 / −0.6	−0.3 / +0.3	+1.7 / −4.1	−47.0	+3.3 / −3.6

TABLE V. The single-differential cross section $d\sigma/dy$ for the reaction $e^+ p \rightarrow e^+ X$. The following quantities are given for each bin: the lower Q^2 cut, the y range, the value at which the cross section is quoted, y_c, and the measured cross section $d\sigma/dy$ corrected to the electroweak Born level. The first uncertainty on the measured cross section is the statistical uncertainty and the second is the systematic uncertainty. The uncertainty on the measured luminosity of 2.5% is not included in the total systematic uncertainty.

Q^2 cut (GeV²)	y range	y_c	$d\sigma/dy$ (pb)
200	0.05–0.10	0.075	$(7.39 \pm 0.06^{+0.08}_{-0.07}) \times 10^3$
	0.10–0.15	0.125	$(5.25 \pm 0.05^{+0.04}_{-0.03}) \times 10^3$
	0.15–0.20	0.175	$(4.06 \pm 0.04^{+0.03}_{-0.04}) \times 10^3$
	0.20–0.25	0.225	$(3.23 \pm 0.04^{+0.03}_{-0.05}) \times 10^3$
	0.25–0.30	0.275	$(2.74 \pm 0.04^{+0.02}_{-0.03}) \times 10^3$
	0.30–0.35	0.325	$(2.38 \pm 0.03^{+0.02}_{-0.03}) \times 10^3$
	0.35–0.40	0.375	$(2.05 \pm 0.03^{+0.03}_{-0.02}) \times 10^3$
	0.40–0.45	0.425	$(1.83 \pm 0.03^{+0.02}_{-0.02}) \times 10^3$
	0.45–0.50	0.475	$(1.63 \pm 0.03^{+0.04}_{-0.02}) \times 10^3$
	0.50–0.55	0.525	$(1.46 \pm 0.03^{+0.05}_{-0.05}) \times 10^3$
	0.55–0.60	0.575	$(1.30 \pm 0.03^{+0.05}_{-0.01}) \times 10^3$
	0.60–0.65	0.625	$(1.19 \pm 0.03^{+0.05}_{-0.03}) \times 10^3$
	0.65–0.70	0.675	$(1.10 \pm 0.03^{+0.05}_{-0.03}) \times 10^3$
	0.70–0.75	0.725	$(9.72 \pm 0.26^{+0.64}_{-0.38}) \times 10^2$

within $\sim \pm 0.5\%$ and approximately constant over the full kinematic range;

(vi) $\{\delta_6\}$ uncertainty in the parton-shower scheme: the systematic uncertainty arising from the choice of parton-shower scheme was estimated by using the MEPS model of LEPTO to calculate the acceptance instead of ARIADNE. The upper and lower limits of the systematic uncertainty were determined by studies of the hadronic-energy flow comparing both MC models with data [37]. The uncertainty was comparable to the statistical uncertainty in a few single-differential bins at high x or low y. It was also significant in a few low-Q^2 double-differential bins at high x, where the statistical uncertainty is small;

(vii) $\{\delta_7\}$ formation of hadronic-energy clusters in the neighborhood of the FCAL beam hole: particles created between the current jet and the proton remnant can leave large energy deposits in the forward calorimeter. Uncertainties in the simulation of the energy flow lead to differences between the reconstructed γ_h in the data and in the simulation, especially at low y. To estimate the systematic uncertainty associated with this effect, the algorithm employed in the measurement of γ_h was modified. In the modified algorithm, energy clusters reconstructed in the forward calorimeter within 30 cm of the beam

TABLE VI. Systematic uncertainties with bin-to-bin correlations for the single-differential cross section $d\sigma/dy$. The left part of the table contains the lower Q^2 cut, the value at which the cross section is quoted, y_c, the measured cross section $d\sigma/dy$ corrected to the electroweak Born level, the statistical uncertainty, and the total systematic uncertainty. The uncertainty on the measured luminosity of 2.5% is not included in the total systematic uncertainty. The right part of the table lists the total uncorrelated systematic uncertainty followed by the bin-to-bin correlated systematic uncertainties δ_1–δ_8 defined in the text. For the latter, the upper (lower) numbers refer to positive (negative) variation of, e.g., the cut value, whereas the signs of the numbers reflect the direction of change in the cross sections.

Q^2 cut (GeV²)	y_c	$d\sigma/dy$ (pb)	Stat. (%)	Total sys. (%)	Uncor. sys. (%)	δ_1 (%)	δ_2 (%)	δ_3 (%)	δ_4 (%)	δ_5 (%)	δ_6 (%)	δ_7 (%)	δ_8 (%)
200	0.075	7.39×10^3	+0.8 / −0.8	+1.1 / −0.9	+0.7 / −0.2	−0.2 / +0.2	+0.0	−0.0 / −0.0	−0.6 / −0.0	−0.3 / +0.3	+0.4 / −0.9	+0.0	−0.2 / +0.2
	0.125	5.25×10^3	+0.9 / −0.9	+0.7 / −0.5	+0.3 / −0.2	−0.2 / +0.1	+0.0	+0.0 / +0.0	−0.2 / +0.5	−0.3 / +0.3	+0.0 / −0.0	−0.3	−0.1 / +0.1
	0.175	4.06×10^3	+1.1 / −1.1	+0.7 / −1.0	+0.3 / −0.3	−0.2 / +0.2	+0.0	+0.0 / +0.0	−0.3 / +0.4	−0.3 / +0.3	+0.3 / −0.8	−0.1	−0.1 / +0.1
	0.225	3.23×10^3	+1.2 / −1.2	+1.0 / −1.7	+0.7 / −0.3	−0.1 / +0.1	+0.0	+0.0 / +0.0	−0.4 / +0.4	−0.3 / +0.3	+0.6 / −1.5	−0.1	−0.0 / +0.1
	0.275	2.74×10^3	+1.3 / −1.3	+0.7 / −0.9	+0.7 / −0.3	−0.1 / +0.1	+0.0	+0.0 / +0.0	−0.5 / +0.4	−0.3 / +0.3	+0.0 / −0.0	−0.3	−0.0 / +0.0
	0.325	2.38×10^3	+1.4 / −1.4	+0.8 / −1.2	+0.5 / −0.4	−0.1 / +0.1	+0.0	−0.0 / +0.1	−0.7 / +0.7	−0.3 / +0.3	+0.2 / −0.5	−0.1	−0.0 / +0.0
	0.375	2.05×10^3	+1.5 / −1.5	+1.4 / −1.0	+0.8 / −0.2	−0.1 / +0.2	+0.0	+0.0 / +0.0	−0.8 / +0.9	−0.3 / +0.3	+0.1 / −0.1	+0.7	−0.0 / −0.0
	0.425	1.83×10^3	+1.6 / −1.6	+1.2 / −0.9	+0.9 / −0.2	−0.1 / +0.2	+0.0	−0.0 / +0.1	−0.7 / +0.8	−0.3 / +0.3	+0.0 / −0.1	−0.4	+0.0 / −0.0
	0.475	1.63×10^3	+1.7 / −1.7	+2.7 / −1.3	+0.5 / −0.6	−0.1 / +0.2	+0.0	−0.1 / +0.1	−0.6 / +2.3	−0.3 / +0.3	+0.4 / −0.9	+1.3	+0.0 / −0.0
	0.525	1.46×10^3	+1.8 / −1.8	+3.3 / −3.5	+0.8 / −0.2	−0.3 / +0.4	+0.0	−0.1 / −0.2	−1.4 / +3.3	−0.3 / +0.3	+0.2 / −0.5	−3.1	+0.0 / +0.0
	0.575	1.30×10^3	+2.0 / −2.0	+3.6 / −1.1	+0.5 / −0.7	−0.5 / +0.5	+0.0	+0.0 / −0.0	−0.5 / +3.3	−0.3 / +0.3	+0.0 / −0.1	+1.2	−0.0 / −0.0
	0.625	1.19×10^3	+2.1 / −2.1	+4.0 / −2.5	+1.0 / −0.4	−1.1 / +1.2	+0.0	−0.1 / −0.3	−1.9 / +3.7	−0.3 / +0.3	+0.3 / −0.7	−0.5	+0.1 / −0.1
	0.675	1.10×10^3	+2.3 / −2.3	+4.6 / −2.6	+0.9 / −0.5	−2.2 / +2.0	+0.0	+0.1 / +0.2	−1.1 / +3.9	−0.3 / +0.3	+0.2 / −0.4	+1.3	+0.1 / −0.1
	0.725	9.72×10^2	+2.7 / −2.7	+6.6 / −3.9	+1.2 / −1.0	−3.1 / +4.4	+0.0	−0.1 / +0.3	−1.3 / +4.2	−0.3 / +0.3	+0.6 / −1.4	+2.4	+0.1 / −0.1

TABLE VII. The reduced cross section $\tilde{\sigma}^{e^+p}$ for the reaction $e^+p \to e^+X$. The following quantities are given for each bin: the Q^2 and x ranges, the values at which the cross section is quoted, Q_c^2 and x_c, and the measured reduced cross section, $\tilde{\sigma}^{e^+p}$, corrected to the electroweak Born level. The first uncertainty on the measured cross section is the statistical uncertainty and the second is the systematic uncertainty. The uncertainty on the measured luminosity of 2.5% is not included in the total systematic uncertainty.

Q^2 range (GeV^2)	x range	Q_c^2 (GeV^2)	x_c	$\tilde{\sigma}(e^+p)$
185–240	$(0.37\text{–}0.60) \times 10^{-2}$	200	0.50×10^{-2}	$1.127 \pm 0.017^{+0.020}_{-0.030}$
	$(0.60\text{–}1.00) \times 10^{-2}$		0.80×10^{-2}	$(9.45 \pm 0.14^{+0.15}_{-0.11}) \times 10^{-1}$
	$(0.10\text{–}0.17) \times 10^{-1}$		0.13×10^{-1}	$(8.16 \pm 0.12^{+0.06}_{-0.09}) \times 10^{-1}$
	$(0.17\text{–}0.25) \times 10^{-1}$		0.21×10^{-1}	$(6.90 \pm 0.12^{+0.07}_{-0.10}) \times 10^{-1}$
	$(0.25\text{–}0.37) \times 10^{-1}$		0.32×10^{-1}	$(5.93 \pm 0.11^{+0.11}_{-0.09}) \times 10^{-1}$
	$(0.37\text{–}0.60) \times 10^{-1}$		0.50×10^{-1}	$(5.28 \pm 0.09^{+0.04}_{-0.11}) \times 10^{-1}$
	$(0.60\text{–}1.20) \times 10^{-1}$		0.80×10^{-1}	$(4.30 \pm 0.07^{+0.23}_{-0.05}) \times 10^{-1}$
	$0.12\text{–}0.25$		0.18	$(3.33 \pm 0.06^{+0.07}_{-0.44}) \times 10^{-1}$
240–310	$(0.60\text{–}1.00) \times 10^{-2}$	250	0.80×10^{-2}	$(9.72 \pm 0.16^{+0.10}_{-0.14}) \times 10^{-1}$
	$(0.10\text{–}0.17) \times 10^{-1}$		0.13×10^{-1}	$(8.30 \pm 0.14^{+0.10}_{-0.07}) \times 10^{-1}$
	$(0.17\text{–}0.25) \times 10^{-1}$		0.21×10^{-1}	$(6.97 \pm 0.14^{+0.12}_{-0.05}) \times 10^{-1}$
	$(0.25\text{–}0.37) \times 10^{-1}$		0.32×10^{-1}	$(5.95 \pm 0.12^{+0.09}_{-0.09}) \times 10^{-1}$
	$(0.37\text{–}0.60) \times 10^{-1}$		0.50×10^{-1}	$(5.28 \pm 0.10^{+0.06}_{-0.09}) \times 10^{-1}$
	$(0.60\text{–}1.20) \times 10^{-1}$		0.80×10^{-1}	$(4.22 \pm 0.07^{+0.22}_{-0.07}) \times 10^{-1}$
	$0.12\text{–}0.25$		0.18	$(3.24 \pm 0.07^{+0.11}_{-0.17}) \times 10^{-1}$
310–410	$(0.60\text{–}1.00) \times 10^{-2}$	350	0.80×10^{-2}	$(9.92 \pm 0.21^{+0.27}_{-0.12}) \times 10^{-1}$
	$(0.10\text{–}0.17) \times 10^{-1}$		0.13×10^{-1}	$(8.23 \pm 0.16^{+0.10}_{-0.14}) \times 10^{-1}$
	$(0.17\text{–}0.25) \times 10^{-1}$		0.21×10^{-1}	$(6.94 \pm 0.16^{+0.06}_{-0.11}) \times 10^{-1}$
	$(0.25\text{–}0.37) \times 10^{-1}$		0.32×10^{-1}	$(6.14 \pm 0.14^{+0.07}_{-0.06}) \times 10^{-1}$
	$(0.37\text{–}0.60) \times 10^{-1}$		0.50×10^{-1}	$(5.10 \pm 0.11^{+0.05}_{-0.08}) \times 10^{-1}$
	$(0.60\text{–}1.20) \times 10^{-1}$		0.80×10^{-1}	$(4.26 \pm 0.08^{+0.07}_{-0.03}) \times 10^{-1}$
	$0.12\text{–}0.25$		0.18	$(3.10 \pm 0.07^{+0.13}_{-0.04}) \times 10^{-1}$
410–530	$(0.60\text{–}1.00) \times 10^{-2}$	450	0.80×10^{-2}	$1.05 \pm 0.02^{+0.04}_{-0.02}$
	$(0.10\text{–}0.17) \times 10^{-1}$		0.13×10^{-1}	$(8.42 \pm 0.22^{+0.11}_{-0.11}) \times 10^{-1}$
	$(0.17\text{–}0.25) \times 10^{-1}$		0.21×10^{-1}	$(6.79 \pm 0.20^{+0.17}_{-0.09}) \times 10^{-1}$
	$(0.25\text{–}0.37) \times 10^{-1}$		0.32×10^{-1}	$(6.30 \pm 0.18^{+0.06}_{-0.16}) \times 10^{-1}$
	$(0.37\text{–}0.60) \times 10^{-1}$		0.50×10^{-1}	$(5.07 \pm 0.13^{+0.09}_{-0.05}) \times 10^{-1}$
	$(0.60\text{–}1.00) \times 10^{-1}$		0.80×10^{-1}	$(4.49 \pm 0.11^{+0.06}_{-0.03}) \times 10^{-1}$
	$0.10\text{–}0.17$		0.13	$(3.64 \pm 0.10^{+0.10}_{-0.04}) \times 10^{-1}$
	$0.17\text{–}0.30$		0.25	$(2.62 \pm 0.08^{+0.04}_{-0.12}) \times 10^{-1}$
530–710	$(0.10\text{–}0.17) \times 10^{-1}$	650	0.13×10^{-1}	$(8.64 \pm 0.20^{+0.24}_{-0.10}) \times 10^{-1}$
	$(0.17\text{–}0.25) \times 10^{-1}$		0.21×10^{-1}	$(7.39 \pm 0.22^{+0.05}_{-0.09}) \times 10^{-1}$
	$(0.25\text{–}0.37) \times 10^{-1}$		0.32×10^{-1}	$(6.32 \pm 0.21^{+0.05}_{-0.19}) \times 10^{-1}$
	$(0.37\text{–}0.60) \times 10^{-1}$		0.50×10^{-1}	$(5.33 \pm 0.18^{+0.05}_{-0.03}) \times 10^{-1}$
	$(0.60\text{–}1.00) \times 10^{-1}$		0.80×10^{-1}	$(4.46 \pm 0.15^{+0.07}_{-0.08}) \times 10^{-1}$
	$0.10\text{–}0.17$		0.13	$(3.53 \pm 0.13^{+0.08}_{-0.04}) \times 10^{-1}$
	$0.17\text{–}0.30$		0.25	$(2.50 \pm 0.09^{+0.08}_{-0.05}) \times 10^{-1}$
710–900	$(0.90\text{–}1.70) \times 10^{-2}$	800	1.30×10^{-2}	$(8.58 \pm 0.24^{+0.25}_{-0.14}) \times 10^{-1}$
	$(0.17\text{–}0.25) \times 10^{-1}$		0.21×10^{-1}	$(7.39 \pm 0.26^{+0.28}_{-0.07}) \times 10^{-1}$
	$(0.25\text{–}0.37) \times 10^{-1}$		0.32×10^{-1}	$(6.61 \pm 0.23^{+0.06}_{-0.15}) \times 10^{-1}$
	$(0.37\text{–}0.60) \times 10^{-1}$		0.50×10^{-1}	$(5.15 \pm 0.18^{+0.11}_{-0.04}) \times 10^{-1}$
	$(0.60\text{–}1.00) \times 10^{-1}$		0.80×10^{-1}	$(4.52 \pm 0.16^{+0.07}_{-0.05}) \times 10^{-1}$
	$0.10\text{–}0.17$		0.13	$(3.60 \pm 0.14^{+0.06}_{-0.05}) \times 10^{-1}$
	$0.17\text{–}0.30$		0.25	$(2.59 \pm 0.12^{+0.14}_{-0.05}) \times 10^{-1}$

TABLE VIII. The reduced cross section $\tilde{\sigma}^{e^+p}$ for the reaction $e^+p \to e^+X$. The following quantities are given for each bin: the Q^2 and x ranges, the values at which the cross section is quoted, Q_c^2 and x_c, and the measured reduced cross section, $\tilde{\sigma}^{e^+p}$, corrected to electroweak Born level. The first uncertainty on the measured cross section is the statistical uncertainty and the second is the systematic uncertainty. The uncertainty on the measured luminosity of 2.5% is not included in the total systematic uncertainty.

Q^2 range (GeV^2)	x range	Q_c^2 (GeV^2)	x_c	$\tilde{\sigma}(e^+p)$
900–1300	$(0.10–0.17) \times 10^{-1}$	1200	0.14×10^{-1}	$(8.47 \pm 0.29^{+0.42}_{-0.26}) \times 10^{-1}$
	$(0.17–0.25) \times 10^{-1}$		0.21×10^{-1}	$(7.90 \pm 0.27^{+0.20}_{-0.14}) \times 10^{-1}$
	$(0.25–0.37) \times 10^{-1}$		0.32×10^{-1}	$(6.59 \pm 0.23^{+0.08}_{-0.20}) \times 10^{-1}$
	$(0.37–0.60) \times 10^{-1}$		0.50×10^{-1}	$(5.41 \pm 0.17^{+0.05}_{-0.11}) \times 10^{-1}$
	$(0.60–1.00) \times 10^{-1}$		0.80×10^{-1}	$(4.60 \pm 0.15^{+0.05}_{-0.04}) \times 10^{-1}$
	$0.10–0.17$		0.13	$(3.56 \pm 0.12^{+0.11}_{-0.03}) \times 10^{-1}$
	$0.17–0.30$		0.25	$(2.42 \pm 0.09^{+0.05}_{-0.04}) \times 10^{-1}$
	$0.30–0.53$		0.40	$(1.38 \pm 0.09^{+0.02}_{-0.15}) \times 10^{-1}$
1300–1800	$(0.17–0.25) \times 10^{-1}$	1500	0.21×10^{-1}	$(6.77 \pm 0.32^{+0.31}_{-0.26}) \times 10^{-1}$
	$(0.25–0.37) \times 10^{-1}$		0.32×10^{-1}	$(6.38 \pm 0.28^{+0.13}_{-0.06}) \times 10^{-1}$
	$(0.37–0.60) \times 10^{-1}$		0.50×10^{-1}	$(5.85 \pm 0.23^{+0.13}_{-0.08}) \times 10^{-1}$
	$(0.60–1.00) \times 10^{-1}$		0.80×10^{-1}	$(4.36 \pm 0.18^{+0.04}_{-0.12}) \times 10^{-1}$
	$0.10–0.15$		0.13	$(3.44 \pm 0.17^{+0.11}_{-0.03}) \times 10^{-1}$
	$0.15–0.23$		0.18	$(3.10 \pm 0.16^{+0.03}_{-0.09}) \times 10^{-1}$
	$0.23–0.35$		0.25	$(2.61 \pm 0.15^{+0.05}_{-0.08}) \times 10^{-1}$
	$0.35–0.53$		0.40	$(1.32 \pm 0.12^{+0.03}_{-0.08}) \times 10^{-1}$
1800–2500	$(0.23–0.37) \times 10^{-1}$	2000	0.32×10^{-1}	$(6.24 \pm 0.33^{+0.23}_{-0.08}) \times 10^{-1}$
	$(0.37–0.60) \times 10^{-1}$		0.50×10^{-1}	$(5.22 \pm 0.26^{+0.06}_{-0.08}) \times 10^{-1}$
	$(0.60–1.00) \times 10^{-1}$		0.80×10^{-1}	$(4.44 \pm 0.21^{+0.09}_{-0.03}) \times 10^{-1}$
	$0.10–0.15$		0.13	$(4.00 \pm 0.22^{+0.07}_{-0.04}) \times 10^{-1}$
	$0.15–0.23$		0.18	$(3.22 \pm 0.19^{+0.03}_{-0.05}) \times 10^{-1}$
	$0.23–0.35$		0.25	$(2.45 \pm 0.17^{+0.04}_{-0.05}) \times 10^{-1}$
	$0.35–0.53$		0.40	$(1.27 \pm 0.13^{+0.02}_{-0.14}) \times 10^{-1}$
2500–3500	$(0.37–0.60) \times 10^{-1}$	3000	0.50×10^{-1}	$(5.43 \pm 0.33^{+0.09}_{-0.09}) \times 10^{-1}$
	$(0.60–1.00) \times 10^{-1}$		0.80×10^{-1}	$(4.12 \pm 0.25^{+0.06}_{-0.08}) \times 10^{-1}$
	$0.10–0.15$		0.13	$(3.50 \pm 0.24^{+0.15}_{-0.04}) \times 10^{-1}$
	$0.15–0.23$		0.18	$(3.17 \pm 0.22^{+0.05}_{-0.11}) \times 10^{-1}$
	$0.23–0.35$		0.25	$(2.29 \pm 0.19^{+0.02}_{-0.11}) \times 10^{-1}$
	$0.35–0.53$		0.40	$(1.35 \pm 0.15^{+0.06}_{-0.05}) \times 10^{-1}$
	$0.53–1.00$		0.65	$(2.02 \pm 0.35^{+0.23}_{-0.13}) \times 10^{-2}$
3500–5600	$(0.40–1.00) \times 10^{-1}$	5000	0.80×10^{-1}	$(4.17 \pm 0.24^{+0.09}_{-0.07}) \times 10^{-1}$
	$0.10–0.15$		0.13	$(3.61 \pm 0.26^{+0.04}_{-0.04}) \times 10^{-1}$
	$0.15–0.23$		0.18	$(2.70 \pm 0.21^{+0.04}_{-0.08}) \times 10^{-1}$
	$0.23–0.35$		0.25	$(2.17 \pm 0.19^{+0.06}_{-0.06}) \times 10^{-1}$
	$0.35–0.53$		0.40	$(1.12 \pm 0.14^{+0.04}_{-0.01}) \times 10^{-1}$
5600–9000	$(0.70–1.50) \times 10^{-1}$	8000	1.30×10^{-1}	$(3.06 \pm 0.29^{+0.08}_{-0.07}) \times 10^{-1}$
	$0.15–0.23$		0.18	$(2.73 \pm 0.28^{+0.03}_{-0.07}) \times 10^{-1}$
	$0.23–0.35$		0.25	$(2.01 \pm 0.24^{+0.08}_{-0.05}) \times 10^{-1}$
	$0.35–0.53$		0.40	$(9.7 \pm 1.7^{+0.5}_{-0.3}) \times 10^{-2}$
	$0.53–1.00$		0.65	$(1.3^{+0.5}_{-0.4}{}^{+0.1}_{-0.1}) \times 10^{-2}$
9000–15 000	$(0.90–2.30) \times 10^{-1}$	12 000	1.80×10^{-1}	$(3.2 \pm 0.4^{+0.1}_{-0.2}) \times 10^{-1}$
	$0.23–0.35$		0.25	$(2.0 \pm 0.4^{+0.0}_{-0.1}) \times 10^{-1}$
	$0.35–0.53$		0.40	$(9.0 \pm 2.3^{+0.6}_{-0.8}) \times 10^{-2}$
15 000–25 000	$0.15–0.35$	20 000	0.25	$(8.8 \pm 2.5^{+0.8}_{-0.2}) \times 10^{-2}$
	$0.35–1.00$		0.40	$(6.3^{+3.8}_{-2.5}{}^{+1.0}_{-1.1}) \times 10^{-2}$
25 000–50 000	$0.25–1.00$	30 000	0.40	$(5.4^{+3.6}_{-2.3}{}^{+0.3}_{-2.3}) \times 10^{-2}$

TABLE IX. Systematic uncertainties with bin-to-bin correlations for the reduced cross section $\tilde{\sigma}^{e^+ p}$. The left part of the table contains the quoted Q^2 and x values, Q_c^2 and x_c, the measured cross section $\tilde{\sigma}^{e^+ p}$ corrected to the electroweak Born level, the statistical uncertainty, and the total systematic uncertainty. The uncertainty on the measured luminosity of 2.5% is not included in the total systematic uncertainty. The right part of the table lists the total uncorrelated systematic uncertainty followed by the bin-to-bin correlated systematic uncertainties δ_1–δ_8 defined in the text. For the latter, the upper (lower) numbers refer to positive (negative) variation of, e.g., the cut value, whereas the signs of the numbers reflect the direction of change in the cross sections.

Q_c^2 (GeV²)	x_c	$\tilde{\sigma}(e^+ p)$	Stat. (%)	Total sys. (%)	Uncor. sys. (%)	δ_1 (%)	δ_2 (%)	δ_3 (%)	δ_4 (%)	δ_5 (%)	δ_6 (%)	δ_7 (%)	δ_8 (%)
200	0.50×10^{-2}	1.13	$^{+1.5}_{-1.5}$	$^{+1.7}_{-2.7}$	$^{+0.5}_{-0.4}$	$^{-0.3}_{+0.4}$	$+0.0$	$^{-0.1}_{-0.1}$	$^{-1.0}_{+1.6}$	$^{-0.3}_{+0.3}$	$^{+0.2}_{-0.4}$	-2.3	$^{+0.0}_{-0.0}$
	0.80×10^{-2}	0.95	$^{+1.4}_{-1.4}$	$^{+1.5}_{-1.2}$	$^{+0.8}_{-0.4}$	$^{-0.1}_{+0.1}$	$+0.0$	$^{-0.0}_{+0.1}$	$^{-0.8}_{+1.0}$	$^{-0.3}_{+0.3}$	$^{+0.2}_{-0.6}$	$+0.8$	$^{-0.0}_{+0.0}$
	0.13×10^{-1}	0.82	$^{+1.4}_{-1.4}$	$^{+0.7}_{-1.1}$	$^{+0.3}_{-0.3}$	$^{-0.1}_{+0.1}$	$+0.0$	$^{+0.0}_{+0.0}$	$^{-0.6}_{+0.5}$	$^{-0.3}_{+0.3}$	$^{+0.3}_{-0.7}$	-0.3	$^{-0.0}_{+0.1}$
	0.21×10^{-1}	0.69	$^{+1.8}_{-1.8}$	$^{+1.0}_{-1.5}$	$^{+0.4}_{-0.6}$	$^{-0.2}_{+0.1}$	$+0.0$	$^{+0.0}_{+0.0}$	$^{-0.3}_{+0.1}$	$^{-0.3}_{+0.3}$	$^{+0.4}_{-0.8}$	-1.2	$^{-0.2}_{+0.2}$
	0.32×10^{-1}	0.59	$^{+1.8}_{-1.8}$	$^{+1.9}_{-1.5}$	$^{+1.2}_{-1.0}$	$^{-0.2}_{+0.1}$	$+0.0$	$^{+0.0}_{+0.0}$	$^{-0.2}_{-0.2}$	$^{-0.3}_{+0.3}$	$^{+0.6}_{-1.5}$	$+0.5$	$^{-0.3}_{+0.3}$
	0.50×10^{-1}	0.53	$^{+1.7}_{-1.7}$	$^{+0.8}_{-2.0}$	$^{+0.5}_{-1.3}$	$^{-0.1}_{+0.2}$	$+0.0$	$^{+0.0}_{+0.0}$	$^{-0.4}_{-0.0}$	$^{-0.3}_{+0.3}$	$^{+0.2}_{-0.5}$	-1.4	$^{-0.4}_{+0.4}$
	0.80×10^{-1}	0.43	$^{+1.5}_{-1.5}$	$^{+5.3}_{-1.1}$	$^{+0.5}_{-0.4}$	$^{-0.1}_{+0.1}$	$+0.0$	$^{+0.0}_{+0.0}$	$^{+0.2}_{+0.1}$	$^{-0.3}_{+0.3}$	$^{+0.8}_{-1.9}$	$+4.8$	$^{-0.4}_{+0.4}$
	0.18	0.33	$^{+1.9}_{-1.9}$	$^{+2.0}_{-13.}$	$^{+1.3}_{-3.4}$	$^{-0.1}_{+0.2}$	$+0.0$	$^{+0.0}_{+0.0}$	$^{+0.1}_{+0.5}$	$^{-0.4}_{+0.4}$	$^{+0.6}_{-1.4}$	-13.0	$^{+0.3}_{-0.3}$
250	0.80×10^{-2}	0.97	$^{+1.7}_{-1.7}$	$^{+1.0}_{-1.4}$	$^{+0.8}_{-0.7}$	$^{-0.2}_{+0.1}$	$+0.0$	$^{+0.0}_{+0.0}$	$^{-0.9}_{+0.7}$	$^{-0.3}_{+0.3}$	$^{+0.1}_{-0.2}$	-0.7	$^{-0.0}_{+0.0}$
	0.13×10^{-1}	0.83	$^{+1.7}_{-1.7}$	$^{+1.2}_{-0.9}$	$^{+0.6}_{-0.2}$	$^{-0.1}_{+0.1}$	$+0.0$	$^{+0.0}_{-0.0}$	$^{-0.5}_{+0.5}$	$^{-0.3}_{+0.3}$	$^{+0.1}_{-0.3}$	$+0.9$	$^{-0.0}_{+0.0}$
	0.21×10^{-1}	0.70	$^{+2.0}_{-2.0}$	$^{+1.8}_{-0.7}$	$^{+0.9}_{-0.3}$	$^{-0.2}_{+0.2}$	$+0.0$	$^{+0.0}_{+0.0}$	$^{+0.3}_{+0.2}$	$^{-0.3}_{+0.3}$	$^{+0.2}_{-0.5}$	$+1.4$	$^{-0.1}_{+0.1}$
	0.32×10^{-1}	0.59	$^{+2.1}_{-2.1}$	$^{+1.6}_{-1.5}$	$^{+0.8}_{-0.5}$	$^{-0.2}_{+0.2}$	$+0.0$	$^{+0.0}_{+0.0}$	$^{-1.1}_{-0.0}$	$^{-0.3}_{+0.3}$	$^{+0.5}_{-1.3}$	$+0.0$	$^{-0.3}_{+0.3}$
	0.50×10^{-1}	0.53	$^{+2.0}_{-2.0}$	$^{+1.2}_{-1.6}$	$^{+1.0}_{-0.4}$	$^{-0.1}_{+0.1}$	$+0.0$	$^{+0.0}_{+0.0}$	$^{-1.0}_{+0.3}$	$^{-0.3}_{+0.3}$	$^{+0.3}_{-0.7}$	-0.8	$^{-0.4}_{+0.4}$
	0.80×10^{-1}	0.42	$^{+1.8}_{-1.8}$	$^{+5.3}_{-1.7}$	$^{+0.4}_{-0.8}$	$^{-0.3}_{+0.2}$	$+0.0$	$^{+0.0}_{+0.0}$	$^{-0.0}_{+0.6}$	$^{-0.3}_{+0.3}$	$^{+1.4}_{-3.3}$	$+4.0$	$^{-0.3}_{+0.4}$
	0.18	0.32	$^{+2.0}_{-2.0}$	$^{+3.4}_{-5.3}$	$^{+0.4}_{-1.6}$	$^{-0.2}_{+0.2}$	$+0.0$	$^{+0.0}_{-0.0}$	$^{-0.6}_{-0.0}$	$^{-0.4}_{+0.4}$	$^{+1.4}_{-3.3}$	-4.8	$^{+0.3}_{-0.3}$
350	0.80×10^{-2}	0.99	$^{+2.1}_{-2.1}$	$^{+2.7}_{-1.2}$	$^{+1.0}_{-0.3}$	$^{-0.2}_{+0.1}$	$+0.0$	$^{+0.0}_{-0.0}$	$^{-0.7}_{+2.6}$	$^{-0.2}_{+0.2}$	$^{+0.1}_{-0.3}$	-0.5	$^{+0.0}_{+0.0}$
	0.13×10^{-1}	0.82	$^{+1.9}_{-1.9}$	$^{+1.3}_{-1.7}$	$^{+1.1}_{-0.3}$	$^{-0.1}_{+0.1}$	$+0.0$	$^{-0.0}_{+0.1}$	$^{-0.7}_{+0.5}$	$^{-0.3}_{+0.3}$	$^{+0.6}_{-1.3}$	$+0.0$	$^{-0.0}_{+0.0}$
	0.21×10^{-1}	0.69	$^{+2.3}_{-2.3}$	$^{+0.9}_{-1.5}$	$^{+0.8}_{-0.9}$	$^{-0.2}_{+0.2}$	$+0.0$	$^{-0.0}_{+0.0}$	$^{-0.5}_{+0.4}$	$^{-0.4}_{+0.4}$	$^{+0.2}_{-0.4}$	-0.8	$^{-0.1}_{+0.1}$
	0.32×10^{-1}	0.61	$^{+2.3}_{-2.3}$	$^{+1.2}_{-0.9}$	$^{+0.9}_{-0.8}$	$^{-0.1}_{+0.2}$	$+0.0$	$^{+0.0}_{+0.0}$	$^{+0.2}_{+0.6}$	$^{-0.3}_{+0.3}$	$^{+0.1}_{-0.2}$	$+0.3$	$^{-0.3}_{+0.3}$
	0.50×10^{-1}	0.51	$^{+2.2}_{-2.2}$	$^{+0.9}_{-1.5}$	$^{+0.9}_{-0.4}$	$^{-0.2}_{+0.3}$	$+0.0$	$^{+0.0}_{-0.0}$	$^{-0.5}_{+0.1}$	$^{-0.3}_{+0.3}$	$^{+0.2}_{-0.4}$	-1.1	$^{-0.4}_{+0.4}$
	0.80×10^{-1}	0.43	$^{+1.9}_{-1.9}$	$^{+1.7}_{-0.7}$	$^{+0.5}_{-0.3}$	$^{-0.2}_{+0.1}$	$+0.0$	$^{+0.0}_{+0.0}$	$^{-0.3}_{+0.6}$	$^{-0.3}_{+0.3}$	$^{+0.2}_{-0.5}$	$+1.4$	$^{-0.3}_{+0.3}$
	0.18	0.31	$^{+2.1}_{-2.1}$	$^{+4.1}_{-1.3}$	$^{+1.9}_{-0.8}$	$^{-0.3}_{+0.2}$	$+0.0$	$^{+0.0}_{+0.0}$	$^{-0.4}_{+0.7}$	$^{-0.3}_{+0.3}$	$^{+0.8}_{-1.8}$	$+2.9$	$^{+0.3}_{-0.2}$
450	0.80×10^{-2}	1.05	$^{+2.3}_{-2.3}$	$^{+3.7}_{-1.9}$	$^{+0.5}_{-0.6}$	$^{-0.7}_{+0.8}$	$+0.0$	$^{-0.0}_{+0.3}$	$^{-0.3}_{+3.6}$	$^{-0.3}_{+0.3}$	$^{+0.1}_{-0.2}$	-1.6	$^{-0.0}_{-0.0}$
	0.13×10^{-1}	0.84	$^{+2.6}_{-2.6}$	$^{+1.2}_{-1.3}$	$^{+1.2}_{-0.4}$	$^{-0.0}_{+0.1}$	$+0.0$	$^{+0.0}_{-0.1}$	$^{-0.5}_{+0.7}$	$^{-0.2}_{+0.2}$	$^{+0.0}_{-0.1}$	-0.8	$^{-0.0}_{+0.0}$
	0.21×10^{-1}	0.68	$^{+3.0}_{-3.0}$	$^{+2.4}_{-1.4}$	$^{+0.7}_{-0.4}$	$^{-0.2}_{+0.1}$	$+0.0$	$^{+0.1}_{+0.1}$	$^{+0.4}_{+0.5}$	$^{-0.2}_{+0.2}$	$^{+0.5}_{-1.2}$	$+2.2$	$^{-0.1}_{+0.1}$
	0.32×10^{-1}	0.63	$^{+2.8}_{-2.8}$	$^{+0.9}_{-2.6}$	$^{+0.8}_{-0.8}$	$^{-0.1}_{+0.2}$	$+0.0$	$^{+0.0}_{+0.0}$	$^{-1.0}_{+0.3}$	$^{-0.3}_{+0.3}$	$^{+0.4}_{-0.9}$	-1.9	$^{-0.2}_{+0.2}$
	0.50×10^{-1}	0.51	$^{+2.6}_{-2.6}$	$^{+1.7}_{-1.0}$	$^{+1.0}_{-0.2}$	$^{-0.2}_{+0.2}$	$+0.0$	$^{+0.0}_{-0.0}$	$^{-0.7}_{+0.3}$	$^{-0.3}_{+0.3}$	$^{+0.1}_{-0.3}$	$+1.3$	$^{-0.3}_{+0.3}$
	0.80×10^{-1}	0.45	$^{+2.5}_{-2.5}$	$^{+1.3}_{-0.6}$	$^{+0.5}_{-0.2}$	$^{-0.2}_{+0.1}$	$+0.0$	$^{+0.0}_{-0.0}$	$^{-0.2}_{+0.2}$	$^{-0.3}_{+0.3}$	$^{+0.1}_{-0.1}$	$+1.2$	$^{-0.2}_{+0.2}$
	0.13	0.36	$^{+2.7}_{-2.7}$	$^{+2.7}_{-1.1}$	$^{+0.6}_{-0.4}$	$^{-0.2}_{+0.1}$	$+0.0$	$^{+0.0}_{-0.1}$	$^{+0.0}_{+0.1}$	$^{-0.4}_{+0.4}$	$^{+0.9}_{-2.1}$	$+1.6$	$^{+0.1}_{-0.1}$
	0.25	0.26	$^{+3.0}_{-3.0}$	$^{+1.6}_{-4.5}$	$^{+0.3}_{-3.2}$	$^{-0.3}_{+0.1}$	$+0.0$	$^{+0.0}_{+0.0}$	$^{+0.1}_{+0.2}$	$^{-0.4}_{+0.4}$	$^{+0.6}_{-1.5}$	-3.0	$^{+0.4}_{-0.5}$
650	0.13×10^{-1}	0.86	$^{+2.4}_{-2.4}$	$^{+2.8}_{-1.1}$	$^{+0.7}_{-0.6}$	$^{-0.1}_{+0.2}$	$+0.0$	$^{-0.1}_{-0.1}$	$^{-0.3}_{+2.6}$	$^{-0.4}_{+0.4}$	$^{+0.4}_{-0.8}$	$+0.6$	$^{-0.0}_{+0.0}$
	0.21×10^{-1}	0.74	$^{+3.0}_{-3.0}$	$^{+0.7}_{-1.2}$	$^{+0.8}_{-0.6}$	$^{-0.1}_{+0.1}$	$+0.0$	$^{+0.1}_{-0.0}$	$^{-0.6}_{-0.1}$	$^{-0.4}_{+0.4}$	$^{+0.1}_{-0.2}$	$+0.3$	$^{-0.1}_{+0.1}$
	0.32×10^{-1}	0.63	$^{+3.4}_{-3.4}$	$^{+0.7}_{-3.0}$	$^{+0.4}_{-0.9}$	$^{-0.3}_{+0.2}$	$+0.0$	$^{-0.0}_{+0.1}$	$^{-0.3}_{+0.4}$	$^{-0.2}_{+0.2}$	$^{+0.4}_{-1.0}$	-2.6	$^{-0.2}_{+0.2}$
	0.50×10^{-1}	0.53	$^{+3.3}_{-3.3}$	$^{+0.9}_{-0.6}$	$^{+0.6}_{-0.4}$	$^{-0.2}_{+0.1}$	$+0.0$	$^{+0.0}_{-0.1}$	$^{+0.1}_{+0.2}$	$^{-0.2}_{+0.1}$	$^{+0.1}_{-0.2}$	$+0.5$	$^{-0.3}_{+0.3}$
	0.80×10^{-1}	0.45	$^{+3.4}_{-3.4}$	$^{+1.6}_{-1.9}$	$^{+0.8}_{-0.6}$	$^{-0.2}_{+0.2}$	$+0.0$	$^{+0.0}_{-0.2}$	$^{-0.4}_{-0.4}$	$^{-0.2}_{+0.2}$	$^{+0.6}_{-1.4}$	-1.5	$^{-0.1}_{+0.1}$
	0.13	0.35	$^{+3.6}_{-3.6}$	$^{+2.3}_{-1.2}$	$^{+0.7}_{-0.8}$	$^{-0.1}_{+0.2}$	$+0.0$	$^{+0.0}_{+0.0}$	$^{-0.6}_{+1.5}$	$^{-0.2}_{+0.2}$	$^{+0.5}_{-1.2}$	$+1.0$	$^{+0.1}_{-0.1}$
	0.25	0.25	$^{+3.8}_{-3.8}$	$^{+3.0}_{-2.1}$	$^{+2.0}_{-1.8}$	$^{-0.1}_{+0.3}$	$+0.0$	$^{+0.0}_{+0.0}$	$^{-0.5}_{+0.8}$	$^{-0.2}_{+0.2}$	$^{+0.8}_{-1.9}$	$+0.8$	$^{+0.4}_{-0.5}$
800	0.13×10^{-1}	0.86	$^{+2.8}_{-2.8}$	$^{+3.0}_{-1.7}$	$^{+1.3}_{-0.6}$	$^{-0.5}_{+0.5}$	-0.1	$^{-0.0}_{+0.4}$	$^{-0.8}_{+2.5}$	$^{-0.3}_{+0.3}$	$^{+0.3}_{-0.8}$	-1.0	$^{-0.0}_{+0.0}$
	0.21×10^{-1}	0.74	$^{+3.6}_{-3.6}$	$^{+3.8}_{-1.0}$	$^{+1.5}_{-0.3}$	$^{-0.2}_{+0.1}$	$+0.0$	$^{-0.0}_{+0.2}$	$^{+0.2}_{+1.8}$	$^{-0.4}_{+0.4}$	$^{+0.3}_{-0.7}$	$+2.9$	$^{-0.1}_{+0.1}$
	0.32×10^{-1}	0.66	$^{+3.5}_{-3.5}$	$^{+0.9}_{-2.3}$	$^{+0.4}_{-1.6}$	$^{-0.1}_{+0.1}$	$+0.0$	$^{-0.1}_{+0.1}$	$^{-0.5}_{+0.6}$	$^{-0.4}_{+0.4}$	$^{+0.1}_{-0.2}$	-1.4	$^{-0.2}_{+0.2}$
	0.50×10^{-1}	0.52	$^{+3.5}_{-3.5}$	$^{+2.2}_{-0.7}$	$^{+1.4}_{-0.3}$	$^{-0.2}_{+0.2}$	$+0.0$	$^{+0.0}_{-0.0}$	$^{+0.9}_{+0.1}$	$^{-0.4}_{+0.4}$	$^{+0.2}_{-0.5}$	$+1.2$	$^{-0.3}_{+0.3}$
	0.80×10^{-1}	0.45	$^{+3.6}_{-3.6}$	$^{+1.4}_{-1.2}$	$^{+0.8}_{-1.0}$	$^{-0.1}_{+0.1}$	$+0.0$	$^{+0.0}_{-0.0}$	$^{+0.3}_{+1.1}$	$^{-0.4}_{+0.4}$	$^{+0.1}_{-0.3}$	$+0.1$	$^{-0.1}_{+0.1}$
	0.13	0.36	$^{+4.0}_{-4.0}$	$^{+1.6}_{-1.5}$	$^{+0.4}_{-0.7}$	$^{-0.0}_{+0.2}$	$+0.0$	$^{+0.0}_{+0.0}$	$^{-1.3}_{+0.0}$	$^{-0.4}_{+0.4}$	$^{+0.1}_{-0.2}$	$+1.4$	$^{+0.1}_{-0.1}$
	0.25	0.26	$^{+4.5}_{-4.5}$	$^{+5.5}_{-2.1}$	$^{+0.5}_{-0.9}$	$^{-0.1}_{+0.1}$	$+0.0$	$^{+0.0}_{+0.0}$	$^{+0.9}_{-0.3}$	$^{-0.2}_{+0.2}$	$^{+1.8}_{-4.2}$	$+3.4$	$^{+0.4}_{-0.5}$

TABLE X. Systematic uncertainties with bin-to-bin correlations for the reduced cross section $\tilde\sigma^{e^+p}$. The left part of the table contains the quoted Q^2 and x values, Q_c^2 and x_c, the measured cross section $\tilde\sigma^{e^+p}$ corrected to the electroweak Born level, the statistical uncertainty, and the total systematic uncertainty. The uncertainty on the measured luminosity of 2.5% is not included in the total systematic uncertainty. The right part of the table lists the total uncorrelated systematic uncertainty followed by the bin-to-bin correlated systematic uncertainties δ_1–δ_8 defined in the text. For the latter, the upper (lower) numbers refer to positive (negative) variation of, e.g., the cut value, whereas the signs of the numbers reflect the direction of change in the cross sections.

Q_c^2 (GeV^2)	x_c	$\tilde\sigma(e^+p)$	Stat. (%)	Total sys. (%)	Uncor. sys. (%)	δ_1 (%)	δ_2 (%)	δ_3 (%)	δ_4 (%)	δ_5 (%)	δ_6 (%)	δ_7 (%)	δ_8 (%)
1200	0.14×10^{-1}	0.85	+3.5 −3.5	+5.0 −3.1	+0.7 −1.1	−0.5 +0.7	−1.5	+0.0 −0.3	−2.3 +3.9	−0.3 +0.3	+0.2 −0.4	+2.8	−0.0 +0.0
	0.21×10^{-1}	0.79	+3.5 −3.5	+2.6 −1.8	+1.2 −0.3	−0.1 +0.1	+0.0	+0.1 +0.3	−1.0 +2.2	−0.3 +0.3	+0.6 −1.4	−0.1	−0.1 +0.1
	0.32×10^{-1}	0.66	+3.5 −3.5	+1.3 −3.0	+0.8 −1.1	−0.0 +0.1	+0.0	−0.1 −0.2	−1.4 +0.6	−0.3 +0.3	+0.9 −2.1	−1.1	−0.2 +0.2
	0.50×10^{-1}	0.54	+3.2 −3.2	+1.0 −2.0	+0.6 −0.5	−0.1 +0.1	+0.0	+0.0 −0.0	−0.4 −0.2	−0.3 +0.3	+0.7 −1.6	−0.9	−0.2 +0.2
	0.80×10^{-1}	0.46	+3.2 −3.2	+1.1 −0.9	+0.8 −0.3	−0.0 +0.2	+0.0	+0.0 +0.0	−0.4 +0.7	−0.3 +0.3	+0.1 −0.3	−0.6	−0.0 +0.1
	0.13	0.36	+3.4 −3.4	+3.2 −1.0	+0.6 −0.2	−0.1 +0.1	+0.0	+0.0 +0.0	+0.7 +0.1	−0.3 +0.3	+0.9 −2.0	+2.3	+0.2 −0.2
	0.25	0.24	+3.9 −3.9	+2.2 −1.6	+0.6 −0.8	−0.1 +0.2	+0.0	+0.0 +0.0	−0.9 +0.1	−0.4 +0.4	+0.8 −1.8	+0.8	+0.4 −0.4
	0.40	0.14	+6.3 −6.3	+1.5 −11.0	+1.1 −6.3	−0.3 +0.2	+0.0	+0.0 +0.0	−1.0 −0.6	−0.5 +0.5	+0.9 −2.1	−8.9	+0.4 −0.4
1500	0.21×10^{-1}	0.68	+4.8 −4.8	+4.6 −3.8	+0.9 −0.9	−0.1 +0.0	+0.6	−0.2 −1.0	−1.5 +4.3	−0.3 +0.3	+0.7 −1.7	−3.0	−0.0 +0.0
	0.32×10^{-1}	0.64	+4.4 −4.4	+2.0 −1.0	+1.1 −0.8	−0.0 +0.1	+0.0	+0.2 −0.2	−0.1 +1.6	−0.3 +0.3	+0.1 −0.2	−0.1	−0.1 +0.1
	0.50×10^{-1}	0.58	+3.9 −3.9	+2.2 −1.3	+1.6 −0.2	−0.1 +0.1	+0.0	+0.1 +0.3	+0.6 +0.4	−0.4 +0.4	+0.5 −1.2	+1.2	−0.2 +0.2
	0.80×10^{-1}	0.44	+4.1 −4.1	+0.8 −2.8	+0.4 −2.2	−0.1 +0.2	+0.0	−0.0 −0.0	−0.1 −0.1	−0.4 +0.4	+0.3 −0.7	−1.6	−0.0 +0.0
	0.13	0.34	+4.9 −4.9	+3.2 −0.9	+1.8 −0.6	−0.1 +0.1	+0.0	+0.0 +0.0	−0.5 +1.1	−0.3 +0.3	+0.0 −0.0	+2.3	+0.2 −0.2
	0.18	0.31	+5.0 −5.0	+1.0 −2.8	+0.8 −0.5	−0.2 +0.2	+0.0	−0.1 +0.0	−0.8 −0.1	−0.3 +0.3	+0.2 −0.4	−2.6	+0.2 −0.2
	0.25	0.26	+5.9 −5.9	+2.0 −3.2	+1.5 −2.5	−0.1 +0.2	+0.0	+0.0 +0.0	−0.4 −0.6	−0.3 +0.3	+0.6 −1.4	−1.5	+0.2 −0.3
	0.40	0.13	+8.7 −8.7	+2.5 −6.1	+2.4 −4.4	+0.1 +0.4	+0.0	+0.0 +0.0	+0.1 −0.3	−0.4 +0.4	+0.3 −0.6	−4.1	+0.3 −0.3
2000	0.32×10^{-1}	0.62	+5.3 −5.3	+3.8 −1.2	+1.0 −1.0	+0.0 +0.1	+1.7	−0.0 +0.1	+0.1 +2.9	−0.4 +0.4	+0.1 −0.1	+1.3	−0.1 +0.2
	0.50×10^{-1}	0.52	+5.0 −5.0	+1.1 −1.6	+0.8 −1.4	−0.1 +0.2	+0.0	−0.1 −0.0	+0.0 −0.3	−0.3 +0.3	+0.2 −0.4	+0.7	−0.2 +0.2
	0.80×10^{-1}	0.44	+4.8 −4.8	+2.0 −0.7	+0.8 −0.4	−0.1 +0.1	+0.0	−0.0 −0.0	+0.7 +0.3	−0.3 +0.3	+0.5 −1.1	+1.1	−0.0 +0.0
	0.13	0.40	+5.5 −5.5	+1.8 −1.1	+1.6 −0.8	−0.3 +0.2	+0.0	−0.0 +0.1	−0.2 +0.4	−0.3 +0.3	+0.2 −0.5	+0.4	+0.2 −0.2
	0.18	0.32	+5.8 −5.8	+0.9 −1.5	+0.5 −1.5	−0.1 +0.3	+0.0	+0.0 +0.0	+0.1 +0.5	−0.4 +0.4	+0.1 −0.3	+0.3	+0.2 −0.2
	0.25	0.24	+7.1 −7.1	+1.6 −2.0	+1.4 −1.4	−0.1 +0.2	+0.0	+0.0 +0.0	−1.0 +0.6	−0.3 +0.3	+0.4 −0.9	+0.3	+0.2 −0.3
	0.40	0.13	+10.0 −10.0	+1.8 −11.0	+1.8 −5.1	−0.4 −0.2	+0.0	+0.0 +0.0	−0.7 +0.4	−0.3 +0.3	+0.1 −0.2	−9.3	+0.3 −0.2
3000	0.50×10^{-1}	0.54	+6.1 −6.1	+1.6 −1.6	+1.3 −1.3	−0.1 +0.2	+0.1	+0.2 +0.2	+0.7 +0.7	−0.3 +0.3	+0.2 −0.5	+0.3	−0.1 +0.1
	0.80×10^{-1}	0.41	+6.0 −6.0	+1.5 −1.9	+1.3 −0.3	−0.1 +0.2	+0.0	−0.1 +0.3	−0.4 −0.6	−0.3 +0.3	+0.2 −0.5	−1.7	+0.0 −0.0
	0.13	0.35	+6.8 −6.8	+4.2 −1.2	+2.7 −0.9	−0.3 +0.1	+0.0	−0.0 +0.1	−0.3 +1.5	−0.3 +0.3	+0.1 −0.3	+2.9	+0.2 −0.2
	0.18	0.32	+6.8 −6.8	+1.4 −3.4	+1.4 −2.9	−0.1 +0.2	+0.0	−0.0 −0.4	−0.0 +0.0	−0.3 +0.3	+0.3 −0.7	−1.6	+0.2 −0.2
	0.25	0.23	+8.4 −8.4	+0.7 −4.6	+0.2 −2.4	−0.1 +0.1	+0.0	+0.0 +0.1	−0.3 +0.1	−0.4 +0.4	+0.2 −0.5	−3.9	+0.2 −0.2
	0.40	0.14	+11.0 −11.0	+4.4 −4.0	+2.5 −1.1	−0.1 +0.0	+0.0	+0.0 +0.0	+0.9 +0.8	−0.3 +0.3	+1.4 −3.4	−3.6	+0.1 −0.2
	0.65	0.02	+18.0 −18.0	+11.0 −6.2	+3.8 −4.9	−0.0 +0.2	+0.0	+0.0 +0.0	−1.8 −1.5	−0.4 +0.4	+2.7 −6.3	+8.6	+1.1 −1.2
5000	0.80×10^{-1}	0.42	+5.7 −5.7	+2.2 −1.6	+1.7 −0.8	−0.1 +0.2	−0.3	−0.5 −0.7	+0.5 +0.8	−0.3 +0.3	+0.4 −1.0	+0.9	+0.1 −0.1
	0.13	0.36	+7.2 −7.2	+1.1 −1.2	+0.5 −0.9	−0.1 +0.1	−0.3	+0.5 +0.2	−0.1 −0.5	−0.3 +0.3	+0.2 −0.4	+0.8	−0.2 +0.2
	0.18	0.27	+7.8 −7.8	+1.5 −3.0	+0.4 −1.8	−0.1 +0.2	−0.3	−0.0 +0.1	−1.0 −0.9	−0.3 +0.3	+0.6 −1.5	−1.7	+0.2 −0.2
	0.25	0.22	+8.8 −8.8	+2.8 −2.8	+0.8 −2.6	−0.1 +0.0	−0.3	+0.0 +0.1	−0.3 −0.5	−0.3 +0.3	+0.6 −1.4	+2.3	−0.1
	0.40	0.11	+12.0 −12.0	+3.5 −1.1	+1.4 −0.7	+0.1 +0.4	−0.3	+0.0 +0.0	−0.1 −0.3	−0.4 +0.3	+0.3 −0.6	+3.1	+0.1 −0.2
8000	0.13	0.31	+9.4 −9.4	+2.6 −2.3	+0.5 −2.1	−0.2 +0.2	−0.3	+0.2 +0.9	+1.7 +0.1	−0.4 +0.4	+0.0 −0.0	+1.6	+0.5 −0.5
	0.18	0.27	+10.0 −10.0	+1.1 −2.4	+0.5 −2.2	−0.2 +0.0	−0.3	−0.1 −0.7	−0.2 +0.8	−0.4 +0.4	+0.2 −0.4	−0.4	+0.2 −0.2
	0.25	0.20	+12.0 −12.0	+3.8 −2.3	+1.7 −2.1	−0.4 +0.3	−0.3	−0.2 +0.2	+0.9 +2.4	−0.3 +0.3	+0.7 −1.7	+1.2	+0.1 −0.2
	0.40	0.10	+17.0 −17.0	+5.0 −3.5	+4.8 −3.3	−0.0 +0.2	−0.3	−0.0 +0.1	+0.4 −0.7	−0.3 +0.3	+0.3 −0.6	+1.0	+0.1 −0.0
	0.65	0.01	+40.0 −30.0	+5.4 −7.2	+4.3 −6.8	−0.4 +0.6	−0.3	+0.0 +0.1	+0.3 −0.4	−0.3 +0.3	+1.3 −3.0	−1.8	+0.8 −0.8
12000	0.18	0.32	+12.0 −12.0	+2.7 −6.6	+2.2 −5.1	−0.6 +0.7	−0.3	−1.4 −3.2	+0.6 +0.7	−0.3 +0.3	+0.9 −2.0	−0.1	+0.3 −0.3
	0.25	0.20	+20.0 −20.0	+1.7 −6.7	+1.3 −5.7	−0.2 +0.1	−0.3	−0.4 +0.7	+0.8 −0.3	−0.4 +0.4	+0.1 −0.3	−3.3	+0.3 −0.3
	0.40	0.09	+25.0 −25.0	+6.7 −8.9	+6.1 −5.7	−0.1 +0.5	−0.3	−0.2 +0.5	−4.6 −0.1	−0.5 +0.5	+1.1 −2.6	−4.9	−0.0 +0.0
20000	0.25	0.09	+28.0 −28.0	+9.5 −2.6	+2.0 −1.9	−0.4 +0.5	−0.3	−1.4 +4.3	+2.9 −0.4	−0.4 +0.4	+0.2 −0.4	+7.7	+0.7 −0.8
	0.40	0.06	+60.0 −40.0	+16.0 −17.	+2.7 −17.	−0.6 +0.5	−0.3	−0.4 +1.5	+1.9 +16.0	−0.3 +0.3	+0.8 −1.8	+0.7	−0.1 +0.2
30000	0.40	0.05	+68.0 −43.0	+5.3 −42.0	+4.3 −2.8	−0.8 +0.3	−0.3	−1.3 −38.0	+2.5 −0.5	−0.4 +0.4	+0.8 −1.8	−19.0	+0.0 −0.1

line were split into their constituent cells and the hadronic quantities recalculated. The effect of the modified algorithm was to give higher values of γ_h in the affected region. The uncertainty obtained was generally small but became comparable to the statistical uncertainty at high x or low y in the single-differential cross sections and in high-x double-differential bins for Q^2 smaller than around 650 GeV^2;

(viii) $\{\delta_8\}$ choice of parton distribution functions: the NC MC events were generated with CTEQ5D PDFs. A set of parton density functions obtained from a ZEUS NLO QCD fit [41], denoted by ZEUS-S, was used to examine the influence of variations in the PDFs on the cross-section measurement. The uncertainties associated with the fit were used to obtain sets of PDFs that correspond to upper and lower uncertainties on the ZEUS-S PDF set. Monte Carlo events were reweighted to the nominal ZEUS-S parton densities and also to the PDFs corresponding to the fit uncertainties, and the cross-section extraction was repeated. The differences between the cross sections obtained using the upper- and lower-uncertainty PDFs and the nominal ZEUS-S parton density function set was taken as the systematic uncertainty arising from the choice of PDFs. The resulting uncertainty was smaller than 1% over the full kinematic range.

C. Single-differential cross sections

The single-differential cross section $d\sigma/dQ^2$ is shown in Fig. 3(a) and tabulated in Table I. The systematic uncertainties are collected in Table II. The SM cross section, evaluated using the ZEUS-S PDFs, gives a good description of the data. The figure also shows the recent ZEUS measurement of $d\sigma/dQ^2$ in e^-p NC DIS, which was also obtained at a center-of-mass energy of 318 GeV [5]. For $Q^2 \gtrsim 3000$ GeV^2, the e^-p cross section is larger than that for e^+p. The relative enhancement of the e^-p cross section over that for e^+p is also clearly demonstrated in Fig. 3(b), where $d\sigma/dx$ is plotted for $Q^2 > 10\,000$ GeV^2 for both e^+p and e^-p NC DIS. This effect is due to the parity-violating part of the Z-exchange contribution which enhances (suppresses) the e^-p (e^+p) cross section over that expected under the assumption of single-photon exchange.

The ratio of $d\sigma/dQ^2$ to the cross section obtained using the ZEUS-S PDFs, as well as the ratios for $d\sigma/dx$ and $d\sigma/dy$ (both for $Q^2 > 200$ GeV^2) are shown in Fig. 4. The plots also contain the SM predictions using the CTEQ6D [42] and MRST(01) [43] PDF sets. The data are well described by the SM using the ZEUS-S PDFs but systematically higher than the predictions of CTEQ6D and MRST(01), although consistent given the luminosity

uncertainty of $\pm 2.5\%$. The cross sections $d\sigma/dx$ and $d\sigma/dy$ are tabulated in Tables III and V (with systematic uncertainties listed in Tables IV and VI).

D. Reduced cross section and the structure function F_2

The reduced cross section, $\tilde{\sigma}^{e^+p}$, tabulated in Tables VII and VIII (with systematic uncertainties listed in Tables IX and X), is shown in Figs. 5 and 6 as a function of x for various values of Q^2. The rise of $\tilde{\sigma}^{e^+p}$ at fixed Q^2 as x decreases reflects the strong rise of F_2 [4]. The SM gives a good description of the data. Also shown are the ZEUS measurements of $\tilde{\sigma}^{e^-p}$. For $Q^2 \lesssim 3000$ GeV^2, the reduced cross sections $\tilde{\sigma}^{e^-p}$ and $\tilde{\sigma}^{e^+p}$ are approximately equal. For $Q^2 \gtrsim 3000$ GeV^2, the Z-boson-exchange contribution causes $\tilde{\sigma}^{e^+p}$ to be smaller than $\tilde{\sigma}^{e^-p}$.
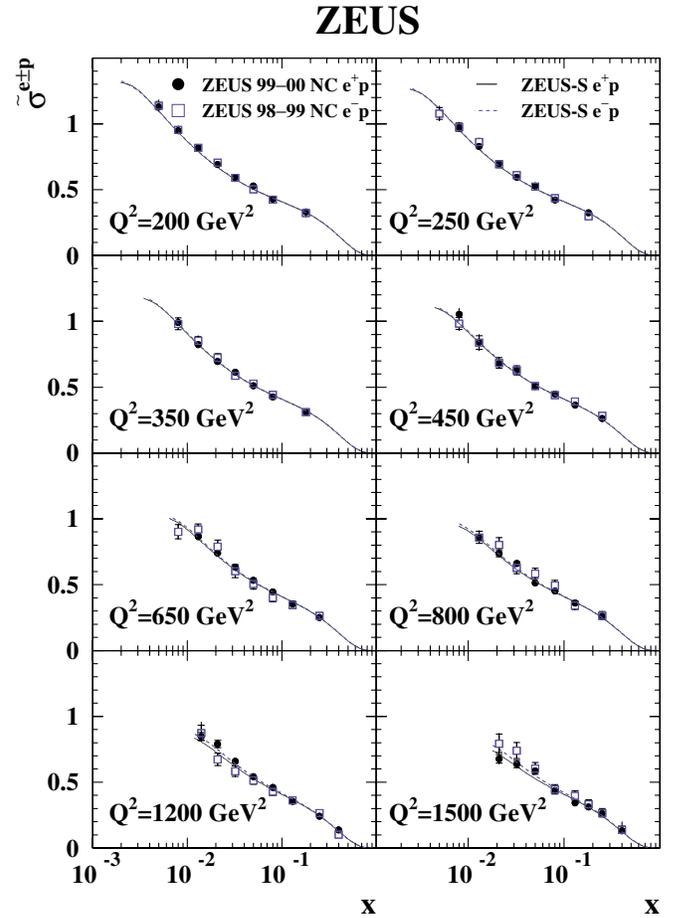
FIG. 5 (color online). The e^+p reduced cross section, $\tilde{\sigma}^{e^+p}$, (solid points) plotted as a function of x at fixed Q^2 between 200 GeV^2 and 1500 GeV^2 compared to $\tilde{\sigma}^{e^-p}$ (open squares). The inner bars show the statistical uncertainty, while the outer ones show the statistical and systematic uncertainties added in quadrature. The Standard Model expectations, evaluated using the ZEUS-S PDFs, are shown as the solid (e^+p) and dashed (e^-p) lines.

ZEUS
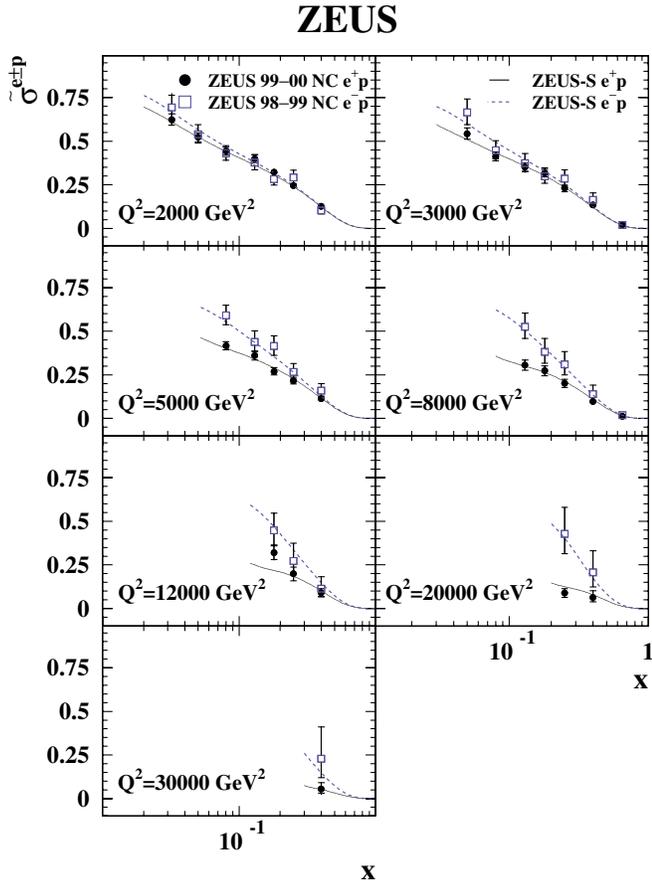
FIG. 6 (color online). The e^+p reduced cross section, $\tilde{\sigma}^{e^+p}$, (solid points) plotted as a function of x at fixed Q^2 between 2000 GeV^2 and 30 000 GeV^2 compared to $\tilde{\sigma}^{e^-p}$ (open squares). The inner bars show the statistical uncertainty, while the outer ones show the statistical and systematic uncertainties added in quadrature. The Standard Model expectations, evaluated using the ZEUS-S PDFs, are shown as the solid (e^+p) and dashed (e^-p) lines.

To compare the present data to measurements from other experiments, the structure function F_2^{em} was extracted from the present data. This was combined with a previous ZEUS measurement of F_2^{em} obtained from data collected at $\sqrt{s} = 300$ GeV [4] in 1996 and 1997.

The reduced cross section includes transverse- and longitudinal-photon as well as Z-boson contributions, which can be expressed as relative corrections in the following way:

$$\tilde{\sigma}^{\,e^+p} = F_2^{\text{em}}(1 + \Delta_{F_2} + \Delta_{xF_3} + \Delta_{F_L}) = F_2^{\text{em}}(1 + \Delta_{\text{all}}),$$

where Δ_{F_2}, Δ_{xF_3}, and Δ_{F_L} correspond to corrections necessary to account for the weak contribution to F_2 and the contributions of the xF_3 and F_L structure functions to the cross section, respectively. The structure function F_2^{em} was obtained by correcting $\tilde{\sigma}^{e^+p}$ for the relative contributions, Δ_{all}, using the CTEQ5D PDFs. The size of the corrections Δ_{all} was typically less than 1% but became as

large as 50% at the highest Q^2. The values of F_2^{em} obtained at the two different center-of-mass energies were combined using

$$F_2^{\text{em}} = \frac{\mathcal{L}_{96/97} F_{2,96/97}^{\text{em}} + \mathcal{L}_{99/00} F_{2,99/00}^{\text{em}}}{\mathcal{L}_{96/97} + \mathcal{L}_{99/00}},$$

where the subscripts on the luminosities ($\mathcal{L}$) and the measured values of F_2^{em} indicate the data-taking periods to which the values correspond. The uncertainties are dominated by the statistical uncertainty. Therefore, correlations between systematic uncertainties were not taken into account when evaluating the uncertainty on the combined F_2^{em}. The separate ZEUS measurements of F_2^{em} from data collected at $\sqrt{s} = 300$ GeV and $\sqrt{s} = 318$ GeV were found to be consistent within their uncertainties.
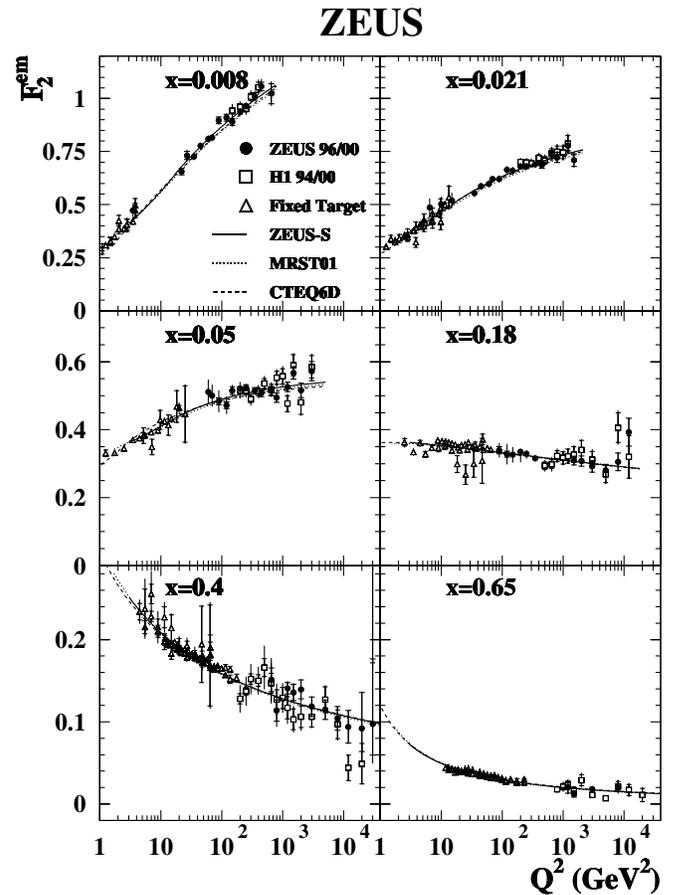
ZEUS

FIG. 7. The structure function F_2^{em} obtained by combining the data presented here with the previous ZEUS measurements as described in the text. The inner bars show the statistical uncertainty, while the outer ones show the statistical and systematic uncertainties added in quadrature. The results of the fixed-target experiments NMC, BCDMS and E665 are plotted as the open triangles while those of the H1 experiment are shown as the open squares.

Figure 7 shows the combined $F_2^{\rm em}$ plotted as a function of Q^2 for several values of x. The results agree well with those obtained by the H1 collaboration [2,3] and with the predictions obtained using the ZEUS-S, CTEQ6D and MRST01 PDFs. The results are also in good agreement with the results obtained at lower Q^2 in fixed-target experiments [31,40,44]. The combined 1996 to 2000 data set corresponds to a luminosity of 93.2 pb^{-1} which is a factor of ~ 3 larger than the luminosity of the previously published data set.

X. SUMMARY

The cross sections for neutral current deep inelastic scattering, $e^+ p \rightarrow e^+ X$, have been measured using 63.2 pb^{-1} of data collected with the ZEUS detector during 1999 and 2000. The single-differential cross sections $d\sigma/dQ^2$, $d\sigma/dx$ and $d\sigma/dy$ have been measured for $Q^2 > 200$ GeV^2. The effect of Z-boson exchange can be clearly seen in $d\sigma/dx$ measured for $Q^2 > 10\,000$ GeV^2. The reduced cross section has been measured in the kinematic range 200 GeV$^2 < Q^2 < 30\,000$ GeV^2 and $0.005 < x < 0.65$. The Standard Model predictions including both γ and Z exchange and using the parton density functions CTEQ6D, ZEUS-S and MRST(01), are in good agreement with the data. The proton structure function $F_2^{\rm em}$ was extracted using the combined $e^+ p$ data sample of 93.2 pb^{-1} taken between 1996 and 2000.

ACKNOWLEDGMENTS

[1] ZEUS Collaboration, J. Breitweg *et al.*, Eur. Phys. J. C **11**, 427 (1999).

[2] H1 Collaboration, C. Adloff *et al.*, Eur. Phys. J. C **13**, 609 (2000).

[3] H1 Collaboration, C. Adloff *et al.*, Eur. Phys. J. C **21**, 33 (2001).

[4] ZEUS Collaboration, S. Chekanov *et al.*, Eur. Phys. J. C **21**, 443 (2001).

[5] ZEUS Collaboration, S. Chekanov *et al.*, Eur. Phys. J. C **28**, 175 (2003).

[6] H1 Collaboration, S. Aid *et al.*, Nucl. Phys. **B470**, 3 (1996)

[7] H1 Collaboration, C. Adloff *et al.*, Nucl. Phys. **B497**, 3 (1997).

[8] H1 Collaboration, C. Adloff *et al.*, Eur. Phys. J. C **19**, 269 (2001).

[9] H1 Collaboration, C. Adloff *et al.*, Eur. Phys. J. C **30**, 1 (2003).

[10] G. Ingelman and R. Rückl, Phys. Lett. B **201**, 369 (1988).

[11] A. M. Cooper-Sarkar, R. C. E. Devenish, and A. De Roeck, Int. J. Mod. Phys. A **13**, 3385 (1998)

[12] ZEUS Collaboration, edited by U. Holm, *The ZEUS Detector*. Status Report (unpublished), DESY (1993), available on http://www-zeus.desy.de/bluebook/bluebook.html

[13] M. Derrick *et al.*, Nucl. Instrum. Methods Phys. Res., Sect. A **309**, 77 (1991); A. Andresen *et al.*, Nucl. Instrum. Methods Phys. Res., Sect. A **309**, 101 (1991); A. Caldwell *et al.*, Nucl. Instrum. Methods Phys. Res., Sect. A **321**, 356 (1992); A. Bernstein *et al.*, Nucl. Instrum. Methods Phys. Res., Sect. A **336**, 23 (1993).

[14] A. Bamberger *et al.*, Nucl. Instrum. Methods Phys. Res., Sect. A **382**, 419 (1996); S. Magill and S. Chekanov, *Proceedings of the IX International Conference on Calorimetry*, edited by B. Aubert, Frascati Physics Series (Annecy, France, 2000), Vol. XXI, p. 625.

[15] A. Dwurazny *et al.*, Nucl. Instrum. Methods Phys. Res., Sect. A **277**, 176 (1989).

[16] N. Harnew *et al.*, Nucl. Instrum. Methods Phys. Res., Sect. A **279**, 290 (1989); B. Foster *et al.*, Nucl. Phys., Sect. B Proc. Suppl **32**, 181 (1993); B. Foster et al. Nucl. Instrum. Methods Phys. Res., Sect. A **338**, 254 (1994);

[17] J. Andruszków *et al.*, DESY-92-066, DESY, 1992; ZEUS Collaboration, M. Derrick *et al.*, Z. Phys. C **63**, 391 (1994); J. Andruszków *et al.*, Acta Phys. Pol. B **32**, 2025 (2001).

[18] A. Kwiatkowski, H. Spiesberger, and H.-J. Möhring, Comput. Phys. Commun. **69**, 155 (1992).

[19] G. A. Schuler and H. Spiesberger, in *Proceedings of the Workshop on Physics at HERA*, edited by W. Buchmüller and G. Ingelman (DESY, Hamburg, Germany, 1991), Vol. 3, p. 1419; H. Spiesberger, HERACLES *and* DJANGOH: *Event Generation for ep Interactions at HERA Including Radiative Processes*, 1998, available on http://www.desy.de/~hspiesb/djangoh.html

[20] CTEQ Collaboration, H. L. Lai *et al.*, Eur. Phys. J. C **12**, 375 (2000).

[21] Particle Data Group, D. E. Groom *et al.*, Eur. Phys. J. C **15**, 1 (2000).

[22] L. Lönnblad, Comput. Phys. Commun. **71**, 15 (1992).

[23] G. Ingelman, A. Edin, and J. Rathsman, Comput. Phys. Commun. **101**, 108 (1997).

[24] T. Sjöstrand, Comput. Phys. Commun. **39**, 347 (1986); T. Sjöstrand and M. Bengtsson, Comput. Phys. Commun. **43**, 367 (1987); T. Sjöstrand, Comput. Phys. Commun. **82**, 74 (1994).

[25] H. Jung, Comput. Phys. Commun. **86**, 147 (1995).

[26] G. Marchesini *et al.*, Comput. Phys. Commun. **67**, 465 (1992).

[27] H. Schnurbusch, Ph.D. thesis, Bonn University (Report BONN-IR-2002-11, 2002).

[28] R. Brun *et al.*, GEANT3, Technical Report CERN-DD/EE/84-1, CERN, 1987;

[29] S. Bentvelsen, J. Engelen, and P. Kooijman, in *Proceedings of the Workshop on Physics at HERA*, edited by W. Buchmüller and G. Ingelman (DESY, Hamburg, Germany, 1992), Vol. 1, p. 23]; K. C. Höger, in *Proceedings of the Workshop on Physics at HERA*, edited by W. Buchmüller and G. Ingelman (DESY, Hamburg, Germany, 1992), Vol. 1, p. 43.

[30] F. Jacquet and A. Blondel, in *Proceedings of the Study for an ep Facility for Europe*, edited by U. Amaldi (DESY, Hamburg, Germany, 1979), p. 391.

[31] BCDMS Collaboration, A. C. Benvenuti *et al.*, Phys. Lett. B **223**, 485 (1989).

[32] M. Moritz, Ph.D. thesis, Universität Hamburg (Report DESY-THESIS-2002-009, 2001).

[33] A. López-Durán Viani, Ph.D. thesis, Humboldt-Universität zu Berlin (Report DESY-THESIS-2001-056, 2001).

[34] A. Kappes, Ph.D. thesis, Bonn University (Report BONN-IR-2001-16, 2001), available at http://www-zeus.physik.uni-bonn.de/german/phd.html

[35] ZEUS Collaboration, S. Chekanov *et al.*, Eur. Phys. J. C **32**, 1 (2003).

[36] W. H. Smith, K. Tokushuku, and L. W. Wiggers, in *Proceedings of the Computing in High-Energy Physics (CHEP), Annecy, France, 1992*, edited by C. Verkerk and W. Wojcik (CERN, Geneva, Switzerland, 1992), p. 222.

[37] J. R. Gonçalo. Ph.D. thesis, Imperial College London (Report DESY-THESIS-2003-022, 2003).

[38] X. Liu, Ph.D. thesis, Columbia University, 2003.

[39] K. Charchula, G. A. Schuler, and H. Spiesberger, Comput. Phys. Commun. **81**, 381 (1994); H. Spiesberger, DJANGO6 *Version 2.4—A Monte Carlo Generator for Deep Inelastic Lepton Proton Scattering Including QED and QCD Radiative Effects*, 1996, available on http://www.desy.de/~hspiesb/django6.html

[40] E665 Collaboration, M. R. Adams *et al.*, Phys. Rev. D **54**, 3006 (1996).

[41] ZEUS Collaboration, S. Chekanov *et al.*, Phys. Rev. D **67**, 012007 (2003).

[42] J. Pumplin *et al.*, J. High Energy Phys. 07 (2002) 012.

[43] A. D. Martin *et al.*, Eur. Phys. J. C **23**, 73 (2002).

[44] NMC Collaboration, M. Arneodo *et al.*, Nucl. Phys. **B483**, 3 (1997).